Topological design principle for the robustness of necroptosis biphasic, emergent, and coexistent (BEC) dynamics

Fei Xu[1,7], Xiang Li[1,2,7,*], Rui Wu[2], Hong Qi[3], Jun Jin[1], Zhilong Liu[1], Yuning Wu[4], Hai Lin[5], Chuansheng Shen[6], Jianwei Shuai[1,2,5,*]

[1]Department of Physics and Fujian Provincial Key Laboratory for Soft Functional Materials Research, Xiamen University, Xiamen 361005, China.

[2]National Institute for Data Science in Health and Medicine and State Key Laboratory of Cellular Stress Biology, Innovation Center for Cell Signaling Network, School of Life Sciences, Xiamen University, Xiamen 361102, China.

[3]Complex Systems Research Center, Shanxi University, Taiyuan 030006, China.

[4]Department of Mathematics and Physics, Fujian Jiangxia University, Fuzhou 350108, China.

[5]Oujiang Laboratory (Zhejiang Lab for Regenerative Medicine, Vision and Brain Health) and Wenzhou Institute, University of Chinese Academy of Sciences, Wenzhou 325001, China

[6]School of Mathematics and Physics, Anqing Normal University, Anqing 246011, China.

[7]These authors contributed equally to this work.

*Correspondence: xianglibp@xmu.edu.cn (X.L.); jianweishuai@xmu.edu.cn (J.S.)

Abstract

Biphasic dynamics, the variable-dependent ability to enhance or restrain biological function, is prevalent in natural systems. Accompanied by biphasic dynamics, necroptosis signaling dominated by RIP1 also appears emergent and coexistent dynamics. Here, we identify the RIP1-RIP3-C8 incoherent feedforward loop embedded with positive feedback of RIP3 to RIP1 is the core topology, and the scale-free feature of RIP3 peak value dictates necroptosis BEC dynamics. Entropy production is introduced to quantify the uncertainty of coexistent dynamics. RIP3 auto-phosphorylation is further determined as a complementary process for robustly attaining necroptosis BEC dynamics. Through screening all possible two- and three-node circuit topologies, a complete atlas of three-node circuit BEC dynamics is generated and only three minimal circuits emerge as robust solutions, proving incoherent feedforward loop is the core topology. Overall, through highlighting a finite set of circuits, this study yields guiding principles for mapping, modulating, and designing circuits for BEC dynamics in biological systems.

Introduction

Biphasic behavior has been observed in a broad range of biological processes to drive essential physiological and developmental functions, such as cell differentiation[1], proliferation[2], and death[3]. Biphasic behavior can be broadly categorized into time-dependent and dose-dependent. Time-dependent biphasic behavior means the output response (*e.g.*, gene expression, protein activation, and ionic concentration, etc.) is increased with time at initial stage but becomes decreased over time. Conversely, the initial decrease and later increase could also be regarded as time-dependent biphasic behavior. Pulse and adaption are the typical time-dependent biphasic behaviors[4-6], such as the transient ERK activation induced by growth factors[6] and the PhoQ activation induced by ADP affinity in bacterial two-component system[7]. Dose-dependent biphasic behavior refers to that the output increases (or decreases) first and then decreases (or increases) with the increase of the input, such as the biphasic dose dependence on Norepinephrine in cyclic AMP signaling[8], and the blue-light-dependent phosphorylation of Arabidopsis cryptochrome 2 in HEK293 cells[9].

Biphasic behavior in biological systems that crosses the tipping point frequently accompanies by the emergence of new patterns. Emergent dynamic is the biological function outcomes of collective interaction among various components, such as the patterns of chimera states and synchronization triggered by cell-to-cell interactions[10,11]. Most recently, we found RIP1 biphasically regulates RIP3 phosphorylation with necroptosis emergence in TNF-induced cell death signaling[12]. However, how the signaling topology is intrinsically related to RIP3 biphasic dynamics with emergence and how the biphasic dynamics are regulated, have not been elucidated. Exploring the link between biological functions and the design principles of biological networks is a fundamental challenge to understand how living organisms can perform various functions efficiently and accurately. The theories of network science have been proven to be powerful tools[13-15]. Despite the apparent complexity and diversity of cell signaling, only a limited number of topologies might be capable of robustly executing particular function. Ma et al. successfully

60 dissected the principle for the design of network topologies that robustly achieve adaptation[4]. Li et

61 al. validated that the robustness of biological oscillators is enhanced by the incoherent inputs[16]. The

62 design principle for robust oscillatory behaviors with respect to noise also have been demonstrated

63 recently[17]. Thus, revealing the properties of how biphasic and emergent dynamics are controlled

64 and tailored in natural systems are urgently needed as well for understanding and optimizing

65 biological regulatory strategies.

66   Starting with searching the essential structure to achieve RIP3 biphasic dynamics with

67 necroptosis emergence, a TNF-induced death circuit model that well reproduces the experimental

68 observations is proposed. The RIP1-RIP3-C8 incoherent feedforward loop is determined to be the

69 core topology for biphasic dynamics with emergence induction, while the positive feedback of RIP1

70 activated by RIP3 dominates the coexistence of necroptosis and apoptosis. A scale-free feature of

71 RIP3 peak value and the Bell-shaped regulation of RIP3 biphasic dynamics are further identified

72 and analyzed. Previous study suggested that scale-free networks are empirically rare[18], and the

73 scale-free feature of RIP3 phosphorylation might be highly related to our recently determined

74 composition of RIP1-RIP3 signaling hub[19]. To quantify the uncertainty of the coexistent dynamics,

75 entropy production of the system is measured through introducing potential landscape and Shannon

76 entropy theories for the first time. Instead of exploring the mechanisms in a specific system, random

77 parameter analysis of the TNF circuit model is also performed, confirming the biphasic dynamics

78 with emergence is the intrinsic properties of the death signaling topology. Besides the positive

79 feedback of RIP1 activated by RIP3, the positive feedback of RIP3 self-activation embedded within

80 the RIP1-RIP3-C8 incoherent feedforward loop is another fundamental structure for achieving the

81 biphasic, emergent, and coexistent (BEC) dynamics. Finally, an exhausting search of all possible

82 two- and three-node network topologies is performed to identify those capable of biphasic dynamics

83 with emergence, and three categories of minimal circuits are obtained. Based on the minimal circuit,

84 an optimal circuit structure for robustly achieving BEC dynamics is further proposed, which is

85 highly consistent with the experimentally observed RIP1-RIP3-C8 circuit. Overall, all the evidence

86 we obtained in this study indicates that the incoherent feedforward loop embedded with positive

87 feedback is a generalizable design principle for the induction of BEC dynamics in diverse biological

88 systems.

89

90 **Results**

91 **Necroptosis BEC dynamics within TNF-induced death circuit**

92 TNF is a multi-functional cytokine that can induce apoptosis or necroptosis depending on cellular

93 contexts[20-22]. The schematic diagram of TNF-induced apoptosis and necroptosis signaling pathway

94 is shown in Figure 1A. To intuitively address the relation of the core module, the reactions, such as

95 association/disassociation, and cascades reaction can be coarsely described to present a conceptual

96 core signaling circuit as shown in Figure 1B. Upon stimulation, TNF combines with TNFR1 to

97 recruit TRADD and RIP1 to form complex-I and then activates them (Figure 1A)[23], which can be

98 simplified as TNF activating TRADD and RIP1 in Figure 1B. The competition between TRADD

99 and RIP1 for binding TNFR1 is described as mutual inhibition[24]. Activation of C8 by sufficient

100 TRADD in complex-II (labeled as C8-IIa) could result in apoptosis. When apoptosis occurs, the

101 cell volume becomes small and the nucleus shrinks[25]. Besides, C8 could also be activated by RIP1

102 in necrosome (labeled as C8-IIb)[26]. In necrosome, C8 inhibits the phosphorylation of RIP1 and

103 RIP3 through cleaving RIP1-RIP3 complex[27]. Phosphorylation of RIP3, the marker of necroptosis[21],

104 also blocks C8 activation by recruiting RSK[28]. RIP1 and RIP3 activate each other through their

105 RHIM-domain, forming a positive feedback loop for the recruitment of MLKL and necroptosis

106 induction[29,30]. As a result, the TNF-induced death dynamics are mainly determined by five

107 components, *i.e.*, activated TRADD (acTRADD), phosphorylated RIP1 (pRIP1), phosphorylated

108 RIP3 (pRIP3), C8 activated by TRADD (C8-IIa), and C8 activated by RIP1 (C8-IIb) (Figure 1B).

109   As the western blotting data shown in Figure 1C, RIP1 knockdown (RIP1 shRNA) accelerates

110   RIP3/MLKL phosphorylation, while RIP1 deletion (RIP1 KO) completely blocks RIP3/MLKL

111   phosphorylation, presenting a biphasic dynamics of necroptosis regulated by RIP1. Decrease of

112   RIP1 also promotes C8 activation, suggesting the suppression role of RIP1 in apoptosis (Figure 1C).

113   To fully understand the essential topology for achieving the biphasic dynamics in the death

114   signaling, a self-evolving ODEs model is constructed based on the circuit shown in Figure 1B

115   (Supplementary Text). The circuit model well reproduces the experimental observations of C8 and

116   RIP3 activation under different RIP1 levels (Figures 1D and 1E). pRIP3 presents an abrupt and

117   large increase at low level of RIP1, triggering the emergent dynamics of necroptosis (Figure 1E).

118   pRIP3 is then gradually reduced with further increase of RIP1. While C8 activation is linearly

119   reduced with RIP1 increase. Experiments show that the deletion of RIP1-induced C8 activation is

120   completely blocked in TRADD deletion cells (Figure 1F), proving that RIP1 suppresses apoptosis

121   through restraining TRADD-dependent C8 activation. Consistently, our circuit model can also

122   quantitatively reproduce the experimental observations and further provides a comprehensive

123   analysis result, showing the decrease of TRADD results in a progressive reduction of C8 activation

124   at varying RIP1 levels (Figure 1G).

125   As RIP3 and C8 can be simultaneously activated (Figure 1C), coexistence death mode of

126   apoptosis and necroptosis in cells could be triggered by proper RIP1 level. Experimental analysis

127   of cell morphology suggests that only necroptosis occurs in wild-type (WT) cells (100% RIP1),

128   while apoptosis can solely be observed in RIP1 deletion cells (0% RIP1) (Figure 1H, upper panel).

129   As expected, both necroptosis and apoptosis can be observed in RIP1-impaired cells. The RIP1-

130   induced cell death mode can be well described by potential landscape theory, which provides a

131   more physical description of the stochastic dynamic and global stability of the biological system[31-

132   33]. Consistent with experimental observations, the middle panel from left to right in Figure 1H are

133   the landscape topography of RIP1 deletion (single apoptosis state), RIP1 impairment (coexistent

134   state of apoptosis and necroptosis), and WT (single necroptosis state) systems that are mapped in

135   the C8-RIP3 phase space. The kinetic pathway (KP) of the system evolving from random initial

136   state (RIS) in the bottom panel of Figure 1H visually presents how the decision of death mode is

137   made under different RIP1 levels. With low or high RIP1 level, cells eventually have a unique death

138   mode of apoptosis or necroptosis. While cells have two mode choices with proper RIP1 level,

139   inducing the coexistent dynamics of apoptosis and necroptosis. Thus, above comparisons confirm

140   that our circuit model has the potential for giving mechanistic insights into the pRIP3/necroptosis

141   BEC dynamics within the TNF-induced death signaling.
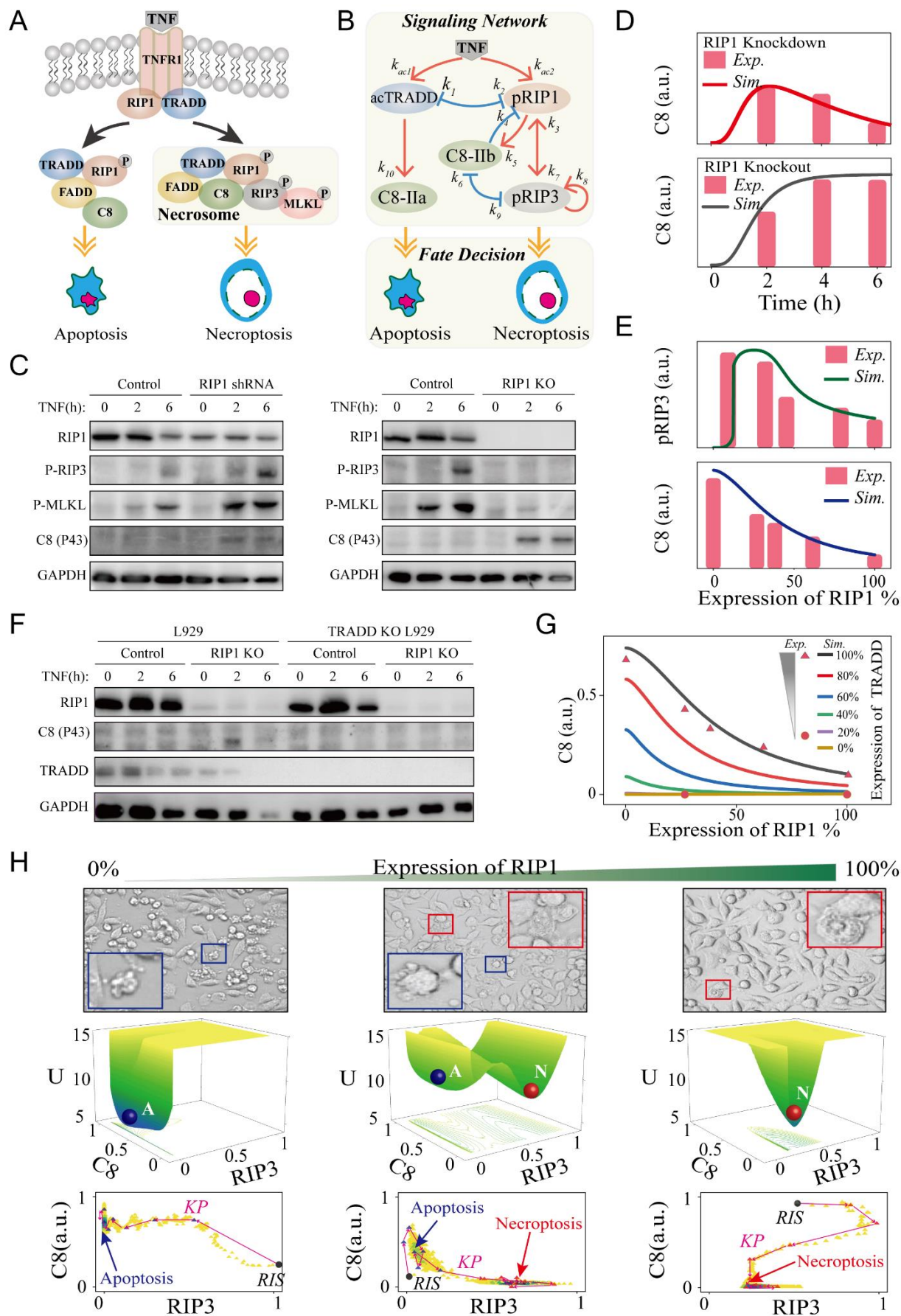
Figure 1. Data-driven modeling of the TNF-induced cell death circuit. (A) Schematic diagram of TNF-induced apoptosis and necroptosis signaling pathway. (B) The coarse-grained signaling network model. (C) Western blot analysis of the effects of RIP1 knockdown (shRNA) or knockout (KO) on indicated proteins activation. (D) Comparison between experimental data (histograms) and simulation results (lines) of the time-course responses of C8 in RIP1 knockdown (upper panel) and RIP1 knockout (down panel) cells. (E) Comparison between experimental data (histograms) and simulation results (lines) of RIP1-dependent pRIP3 response (upper panel) and C8 activation response (down panel). (F) Western blot analysis of TRADD knockout on indicated protein activation for wildtype and RIP1 knockout cells. (G) Comparison between experimental data (dots) and simulation results (lines) of the effect of TRADD level on RIP1-dependent C8 activation. (H) Cell morphologies under different expression levels of RIP1. The red and blue boxes indicate the represented apoptotic and necroptotic cells, respectively. Potential landscape reveals switch in cell death modes under different levels of RIP1 and the corresponding kinetic pathways (KP) of system evolution from random initial states (RIS).

RIP1-RIP3-C8 incoherent feedforward loop determines necroptosis BEC dynamics

To dissect the essential topology for the BEC dynamics of pRIP3 induced by RIP1, roles of TRADD and C8 are first explored. Biphasic and emergent (BE) dynamics of pRIP3 are not affected by TRADD deletion (Figure 2A, blue line), but disappear in the absence of C8 (Figure 2A, green line), implying that C8 is the essential node for BE dynamics. Deletion of C8 barely affects the emergence of pRIP3, and pRIP3 level keeps constant with further increase of RIP1. Thus, the dynamics of pRIP3 consists of two processes: when RIP1 increases from 0 to a low critical level (~10% RIP1), pRIP3 increases abruptly, inducing the emergent dynamics of necroptosis. While with the increase of RIP1, inhibition of C8 on pRIP3 takes effect, causing pRIP3 gently decreases.

168   Then, the nine interaction terms among RIP1, RIP3, and C8 in the irreducible circuit model

169   are respectively removed to determine the essential terms (Figure 2B). BE dynamics disappear

170   when the terms including k_5 (C8 activated by RIP1), k_7 (RIP3 activated by RIP1), and k_9 (RIP3

171   inhibited by C8) are respectively set to 0, while BE dynamics are still observed when the other six

172   terms are fixed to 0. We introduced the coefficient H, which is defined as $H = (pRIP3_{Peak}-$

173   $pRIP3_{RIP1\_100\%}) / pRIP3_{tot}$ to quantify the scale of biphasic dynamics. $pRIP3_{Peak}$ is the maximum

174   level of pRIP3, and $pRIP3_{RIP1\_100\%}$ is the level of pRIP3 when the expression level of RIP1 is 100%

175   (wild-type). Therefore, analysis in Figure 2B indicates that the essential topology for necroptosis

176   BE dynamics of the TNF-induced death circuit is constituted by the incoherent feedforward loop

177   structure (k_5, k_7, and k_9) that are embedded in the three nodes (RIP1, RIP3, and C8).

178   Besides the identified RIP1-RIP3-C8 topological structure for BE dynamics, the interaction

179   term required for achieving the coexistence mode of necroptosis and apoptosis is further explored

180   based on potential landscape analysis. We respectively removed the terms besides the identified

181   essential topology for BE dynamics to determine whether apoptosis and necroptosis states could

182   coexist with RIP1 variation. As shown in Figure 2C, only when the term of RIP1 activated by pRIP3

183   (k_3) is removed (Figure 2Ciii), the system presents solely one potential well with high C8 and low

184   pRIP3 level. While the system still exhibits two coexisting wells with the blockage of other terms.

185   Taken together, as the diagram shown in Figure 2D, RIP1-RIP3-C8 incoherent feedforward loop

186   embedded with the positive feedback of RIP3 to RIP1 is the core topological structure for achieving

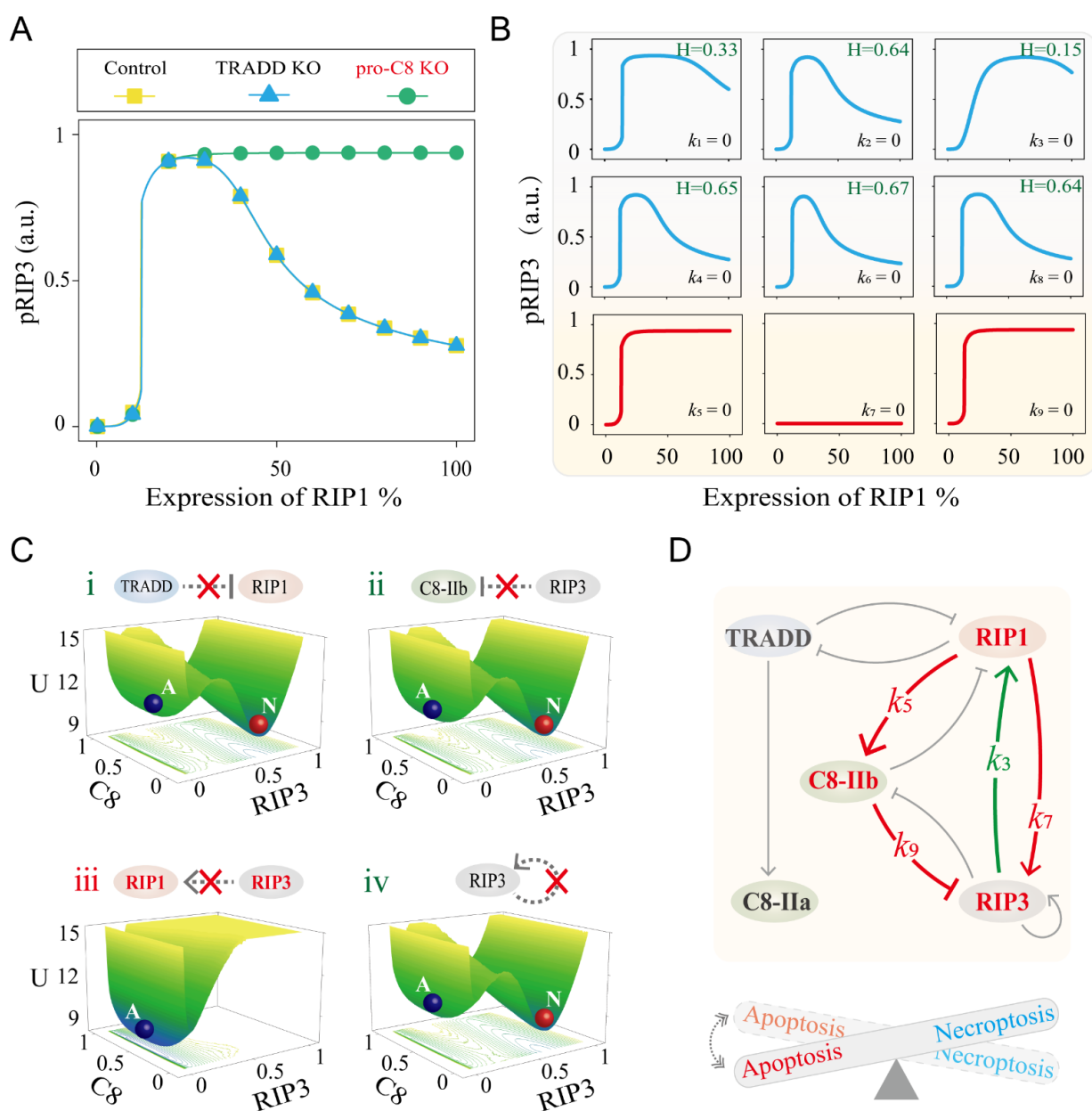187   RIP1-induced necroptosis BEC dynamics.

Figure 2. Identification of the core structure for pRIP3/necroptosis BEC dynamics. (A) Comparison of pRIP3 BE dynamics under control, TRADD KO, and C8 KO conditions. (B) The dynamics of pRIP3 when any one of the nine interaction terms in circuit model is removed, respectively. (C) Potential landscapes of the system when the four interaction terms are severally removed. (D) Summary of the constituents and terms that can achieve BE dynamics (red lines) with coexistent death mode (green line).

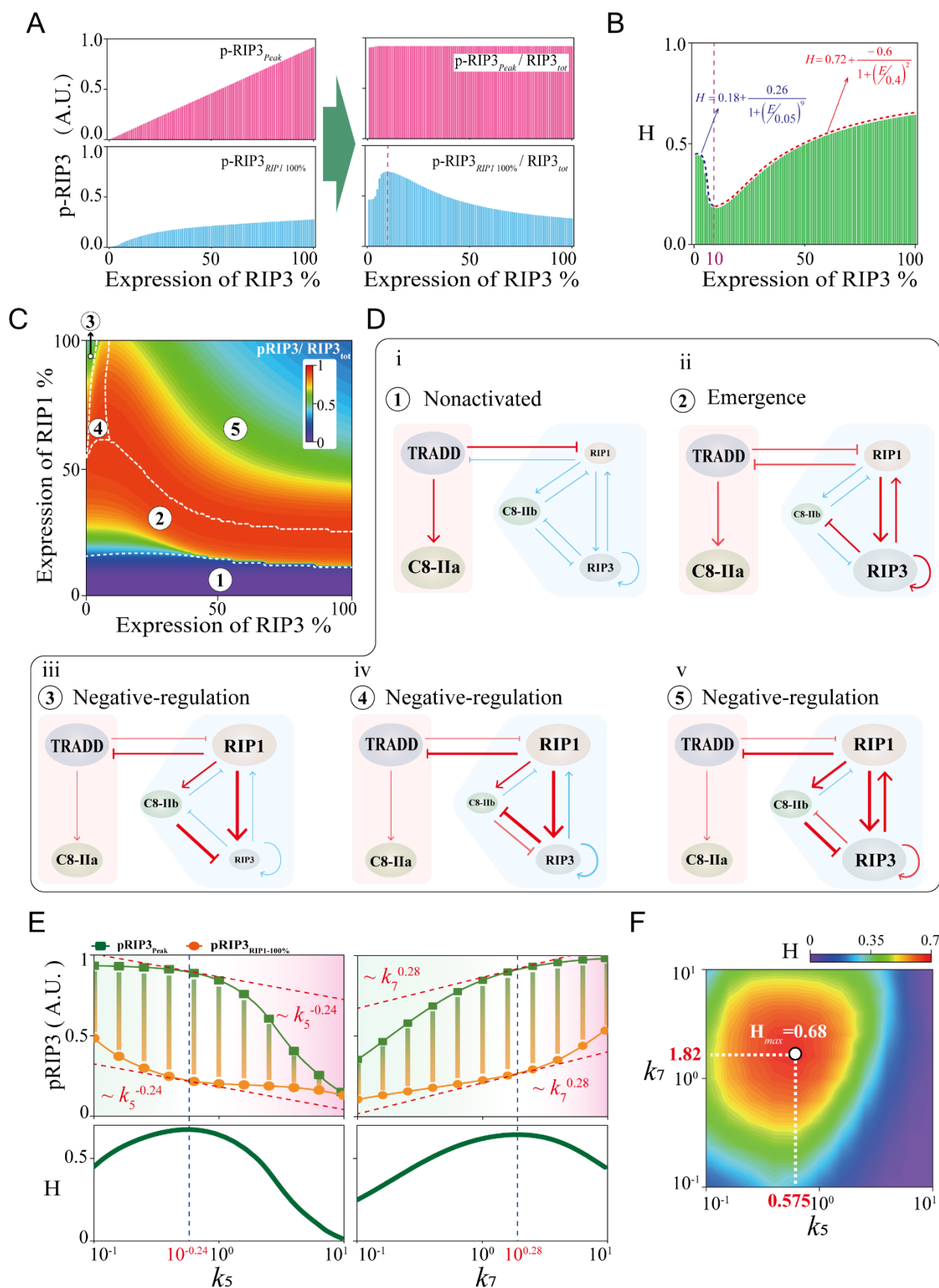**Bell-shaped regulation of necroptosis biphasic dynamics by RIP3 and the feedforward terms**

Having identified the essential topological structure, we next explored the control mechanism of

how necroptosis biphasic dynamics is generated and regulated by the protein nodes (RIP3, TRADD,

and C8) and interaction terms. Both the absolute and relative levels of $pRIP3_{Peak}$ and $pRIP3_{RIP1\_100\%}$

to RIP3 expression level variation are shown in Figure 3A. The absolute level of $pRIP3_{Peak}$ is

linearly positively correlated with RIP3 (upper left panel of Figure 3A), whereas the relative level

of $pRIP3_{Peak}$ ($pRIP3_{Peak}/RIP3_{tot}$) remains constant, presenting a scale-free feature (upper right panel

of Figure 3A). For $pRIP3_{RIP1\_100\%}$, the absolute level is also positively related to RIP3, but the

relative level exhibits a biphasic behavior (down panel of Figure 3A). The scale-free feature of

$pRIP3_{Peak}$ and biphasic behavior of $pRIP3_{RIP1\_100\%}$ result in the biphasic dynamics of RIP3 presents

inverted Bell-shaped responses to RIP3 expression level, as the quantified scale of biphasic

dynamics H shown in Figure 3B. Four-Parameter Logistic Function is considered for a piecewise

fit of H. When RIP3 is lower than ~10%, H decreases monotonically from the maximum value of

0.44 to 0.18, and the decline rate is the largest at ~5%. Conversely, H is positively correlated with

RIP3 when RIP3 is higher than ~10%. The fitted function suggests that the maximum value of H

cannot exceed 0.72 with a maximum increase rate at ~40%.

To systematically reveal the Bell-shaped regulation mechanism of RIP3 on the scale of H, the

variation of relative pRIP3 ($pRIP3/RIP3_{tot}$) is investigated in RIP3-RIP1 phase plane (Figure 3C).

The plane can be divided into 5 regions with specific regulatory mechanisms. Region 1 indicates

that the inhibition of TRADD on RIP1 is dominant and RIP3 remains inactive with low expression

level of RIP1 (Figure 3Di). When RIP1 increases to a critical level, RIP1 activated RIP3 and the

self-activation of RIP3 induce the emergence of pRIP3 (Figure 3Dii), corresponding to region 2.

Regions 3, 4, and 5 show that high level of RIP1 negatively regulates pRIP3. In region 3 with the

low expression level of RIP3, pRIP3 is greatly restrained by C8 (Figure 3Diii), exhibiting a large

value of H. As the expression level of RIP3 increases in region 4, inhibition of pRIP3 on C8

222   gradually becomes dominant (Figure 3Div). pRIP3 level increases and H decreases. Further

223   increase of RIP3 in region 5 enhances the positive feedback of pRIP3 on RIP1, which indirectly

224   promotes the inhibition of C8 on pRIP3 (Figure 3Dv), resulting in a resurgence of the large scale

225   of biphasic dynamics (large value of H). We confirmed the inferences though respectively reducing

226   the strength of the corresponding interaction terms, which characterize the mutual inhibition

227   between C8 and pRIP3, and the positive feedback of pRIP3 on RIP1 (Figure S1A). Specifically,

228   when the strength of C8 inhibition on RIP3 (k_6) decreases, region 3 disappears and the relative level

229   of pRIP3 in region 5 increases. While weakening the inhibition strength of pRIP3 on C8 (k_9) results

230   in the disappearance of region 4 and the expansion of region 3. Attenuating the positive feedback

231   strength of pRIP3 on RIP1 (k_3) increases the relative level of pRIP3 in region 5. The scale of

232   biphasic dynamics H is barely influenced by TRADD (Figure S1B), but is gradually enhanced with

233   the increase of C8 (Figure S1C). For C8, the relative $pRIP3_{Peak}$ also presents a scale-free feature,

234   while the relative $pRIP3_{RIP1\_100\%}$ is linearly decreased with the increase of C8.

235   We next investigated the role of interaction terms in mediating the scale of biphasic dynamics

236   H. Among the nine terms, only k_5 (C8 activated by RIP1) and k_7 (RIP3 activated by RIP1) that

237   involves in the RIP1-RIP3-C8 incoherent feedforward loop, can both mediate the levels of

238   $pRIP3_{Peak}$ and $pRIP3_{RIP1\_100\%}$, achieving Bell-shaped regulation on H (Figure 3E and S2). With the

239   increase of k_5, $pRIP3_{Peak}$ decreases first slow and then fast, while $pRIP3_{RIP1\_100\%}$ decreases first fast

240   and then slow, presenting distinct responses (Figure 3E). In contrast, increase of k_7 makes $pRIP3_{Peak}$

241   to increase first fast and then slow, but $pRIP3_{RIP1\_100\%}$ to increase first slow and then fast. The scale

242   H is the largest when the change rate of $pRIP3_{Peak}$ and $pRIP3_{RIP1\_100\%}$ are equal with the

243   corresponding strengths $k_5=10^{-0.24}$ and $k_7=10^{0.28}$. $pRIP3_{Peak}$ can hardly be regulated by the rest seven

244   terms, while $pRIP3_{RIP1\_100\%}$ is positively regulated by k_6 and negatively regulated by k_1, k_3, and k_9

245   (Figure S2A). Further two-parameters phase plane analysis indicates that the maximum value of H

246   is 0.68 when $k_5=0.575$ and $k_7 =1.82$ (Figure 3F). We severally profiled $pRIP3_{Peak}$ and $pRIP3_{RIP1\_100\%}$

247   in the k_5-k_7 phase plane (Figure S3A), and three different regions and two processes are identified

248   in the plane to reveal the mechanism of Bell-shaped regulation (Figure S3B). Although the term of

249   k_9 (inhibition of C8 on pRIP3) that involves in the RIP1-RIP3-C8 incoherent feedforward loop can

250   not drive Bell-shaped regulation on H, k_9 significantly amplifies the Bell-shaped regulation of k_5

251   (C8 activated by RIP1) or k_7 (RIP3 activated by RIP1) on H (Figure S3C).

Figure 3. Scale-free emergence of pRIP3 and Bell-shaped regulation of necroptosis biphasic dynamics. (A) The variation of absolute and relative levels of $pRIP3_{Peak}$ and $pRIP3_{RIP1\_100\%}$ with RIP3 expression level increases. (B) The quantified scale H of pRIP3 biphasic dynamics. (C) The relative level of pRIP3 in the RIP3-RIP1 phase plane, giving the plane divided into 5 regions. (D) Topological analysis of the regulatory mechanisms of the 5 regions in (C). (E) Analysis of the k_5 and k_7 Bell-shaped regulation on pRIP3 biphasic dynamics. (F) Phase diagram of H in k_5-k_7 parameter spaces.
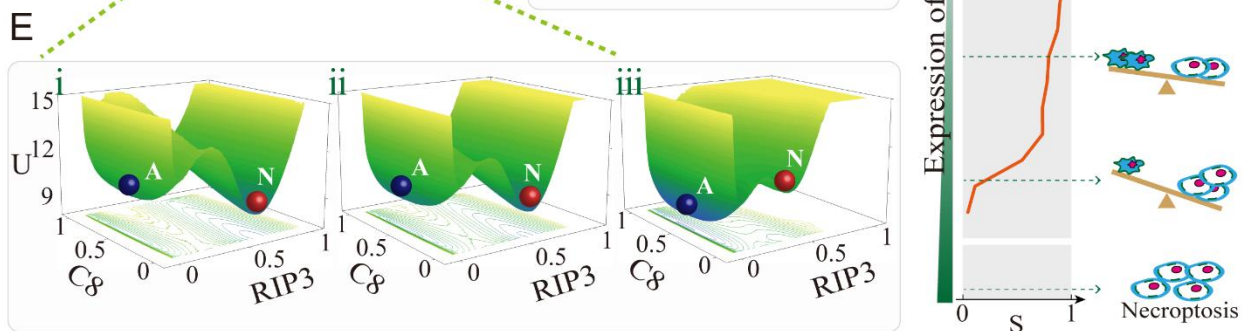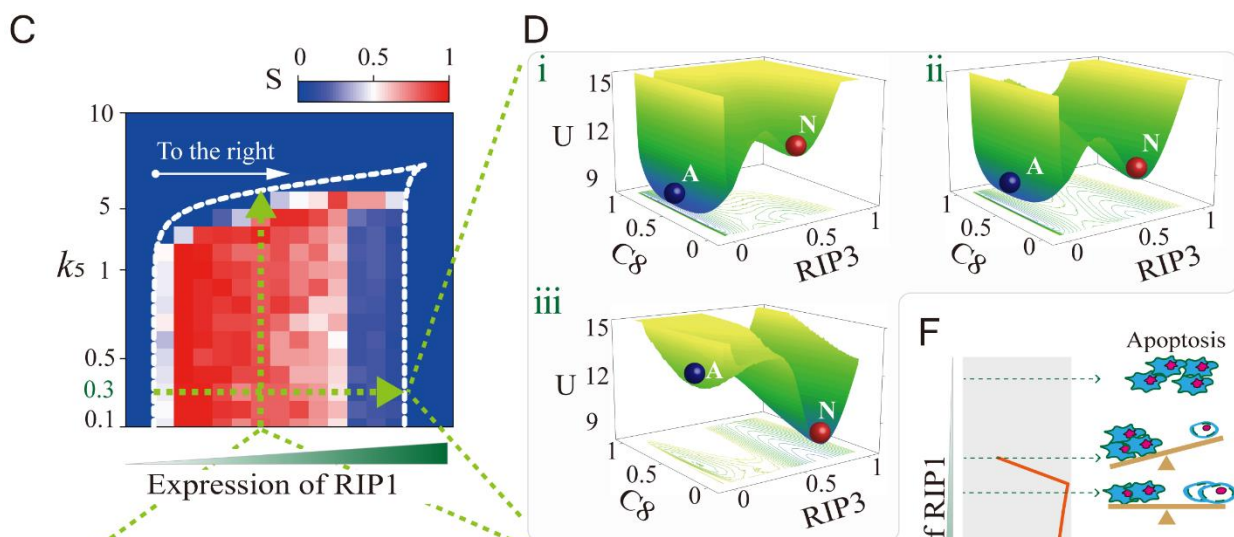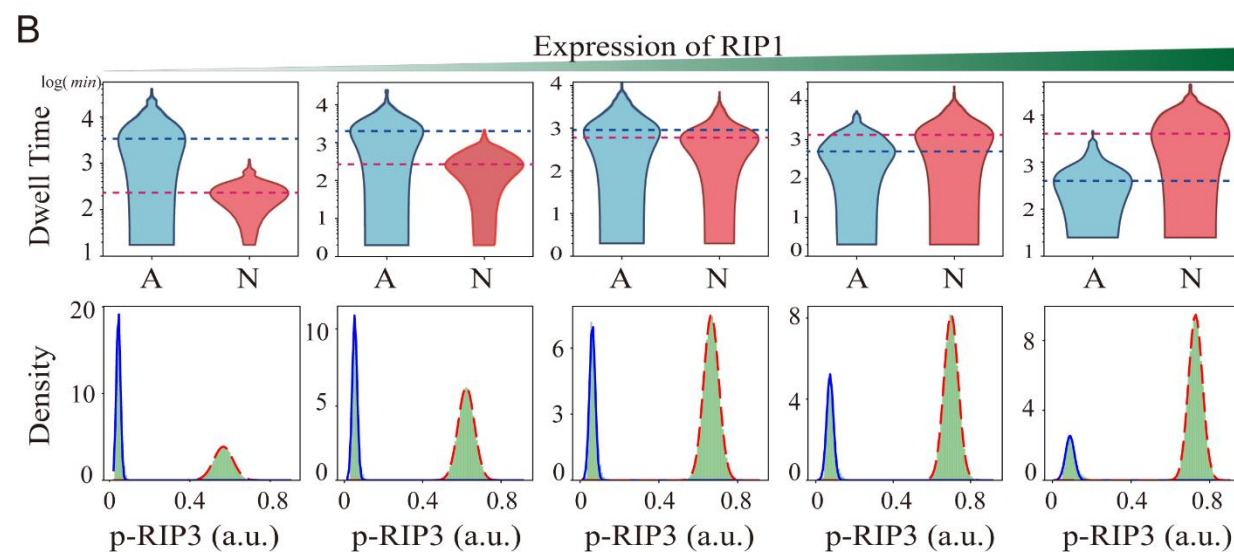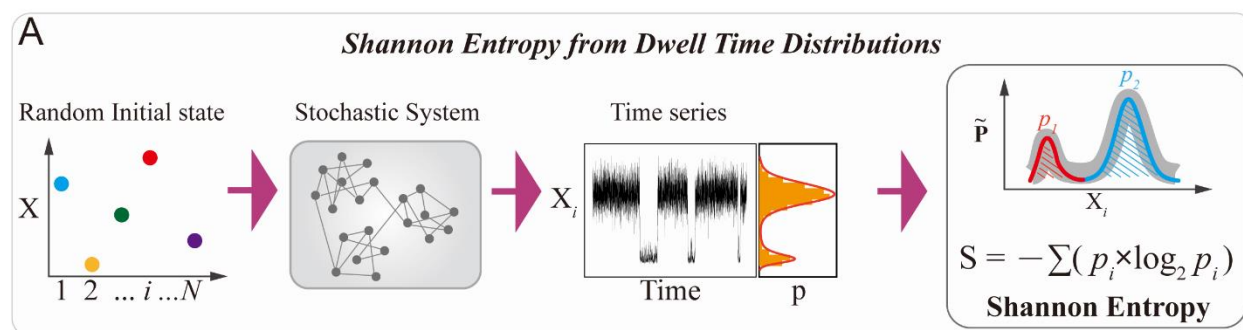

Shannon entropy quantifies uncertainty of the coexistence death modes

Previous studies attempted to infer the information for thermodynamic quantities by observing dwell time distribution of transitions among multiple steady states[34-37]. The cell death signaling presents coexistent dynamics with proper RIP1 level, as the two basins (apoptosis and necroptosis) shown in the death landscape topography (Figure 1G). To measure the uncertainty of cell fate decision, we introduced Shannon entropy to estimate entropy production, which is defined as $S = -\Sigma p_i log_2(p_i)$. p_i is the probability of the i-th death mode, and i represents the state of apoptosis or necroptosis. S characterizes the degree of disorder of the cell death system. The larger the value of S is, the more disorder the system is. Figure 4A illustrates the analysis procedure for Shannon entropy by calculating dwell time distribution. Stochastic cell death system is obtained by adding Gaussian white noise to the deterministic system with random initial states. Temporal dynamics of the system are precisely recorded at the free degrees of pRIP3 to obtain the dwell time distribution of the system in different states. With the increase of RIP1, the dwell time in apoptosis state is gradually decreased, but is increased in necroptosis state (Figure 4B, upper panel), and the corresponding dwell time distributions are shown as well (Figure 4B, down panel).

Shannon entropy of k_5 (term of C8 activated by RIP1 that exhibits Bell-shaped regulation on necroptosis biphasic dynamics) in regulating RIP1-dependent coexistent dynamics is measured

278   (Figure 4C). The region surrounded by the white dotted line is the coexistence transition region.

279   The color code in the transition region indicates the degree of transition between apoptosis and

280   necroptosis of the system. The system presents a highly disordered state when RIP1 is near the level

281   to induce pRIP3/necroptosis emergent dynamics. Shannon entropy (S) gradually decreases and

282   necroptosis becomes dominated with further increase of RIP1. Thus, the cell fate switches from

283   ordered apoptosis to highly disordered and finally to ordered necroptosis with the increase of RIP1.

284   A more intuitive potential landscape topography transition is shown in Figure 4D when k_5 is fixed

285   at the standard value of 0.3. With the increase of RIP1, the depth of the apoptosis basin is gradually

286   decreased, while the necroptosis basin is increased, suggesting that RIP1 biases the cell fate towards

287   necroptosis. The transitions of Shannon entropy and potential landscape topography with different

288   k_5 are also investigated with RIP1 is fixed at 11% (Figure 4E). In contrast to RIP1, increase of k_5

289   results in the uncertainty of cell fate switches from highly disordered to ordered apoptosis, giving

290   the depth of apoptosis basin increased and necroptosis basin decreased. The entropy result also

291   reveals that the increase of k_5 causes a high level demand for RIP1 to trigger pRIP3 emergent

292   dynamics (white arrow in Figure 4C). The larger the value of k_5 is, the higher RIP1 level is required

293   for inducing necroptosis emergent dynamics.

294   Therefore, acting as the driving force, RIP1 makes the system dynamics like a "seesaw"

295   (Figure 4F). The system exclusively executes apoptosis at low RIP1 level. Increase of RIP1

296   significantly elevates pRIP3 level and entropy production. The death system is highly disordered

297   and will selectively undergo apoptosis or necroptosis, depending on the initial conditions. High

298   level of RIP1 reduces entropy production and drives the system to ordered necroptosis. RIP1-

299   dependent coexistent dynamics regulated by the other three reactions within the identified essential

300   topological structure (Figure 2D) are shown in Figure S4, indicating that the terms of k_3 (RIP1

301   activated by pRIP3) and k_7 (RIP3 activated by RIP1) can efficiently switch death modes, while the

302   system remains highly disordered with the variation of k_9 (inhibition of C8 on pRIP3).

303

304

305 **Figure 4. Shannon entropy quantifies the uncertainty of cell fate decisions.** (A) Illustration of

306 the calculation procedure of Shannon entropy with dwell time distribution. (B) Statistics and

307 distribution of dwell time under five representative RIP1 expression levels at the free degrees of

308 pRIP3. (C) The quantified Shannon entropy of k_5 in regulating RIP1-dependent coexistent

309 dynamics. (D) and (E) The potential landscape topography of coexistent death modes with k5=0.3,

310 and RIP1 level at 10%, 11%, and 12.5% respectively (D), and the level of RIP1 at 11% with k5=0.1,

311 0.5, and 0.7 respectively (E). (F) Shannon entropy characterizes the uncertainty of cell fate, and a

312 diagram of "seesaw" that reflects the death modes decision under different RIP1 levels.

313

314 **Random circuit analysis identifies two core topologies for necroptosis BEC dynamics**

315 **induction**

316 To avoid the fortuity of deterministic model with specific parameters, random circuit analysis is

317 further performed to identify the core topology for necroptosis BEC dynamics. Latin hypercube

318 sampling is used to obtain uniform random parameter regimes within reasonable biological

319 interval[4,12,38], and all parameter regimes that can achieve BE, and BEC dynamics are screened

320 (Figure 5A). We assumed that the biphasic dynamics (BD) of pRIP3 satisfies *pRIP3$_{Peak}$* is higher

321 than *pRIP3$_{RIP1\_100\%}$* by more than 1%, *i.e.*, BD is defined when BD=(*pRIP3$_{Peak}$* -

322 *pRIP3$_{RIP1\_100\%}$*)/*pRIP3$_{Peak}$* >=1%. Since pRIP3 presents an abrupt and large increase at low level of

323 RIP1 (Figure 2A), emergent dynamics (ED) is also considered through satisfying pRIP3 is

324 increased by more than 50% when RIP1 continuously increases by 10% (ED=$\Delta pRIP3$/$\Delta RIP1$>=5).

325 　　The probabilities under five representative RIP3 expression levels are firstly calculated, and

326 50,000 groups of random samples are taken for each RIP3 level. The probabilities of achieving BE

327 dynamics (blue histograms) and BEC dynamics (green histograms) are presented in Figure 5B. As

328 the result indicated, the vast majority (~86.6%) of samples that achieve BE also have coexistent

329 dynamics, revealing that the necroptosis BE dynamics is highly related to coexistence of death

330   mode. The probabilities of BE and BEC dynamics decrease monotonically with RIP3 decreases.

331   The probability of only considering biphasic dynamics is decreased by 17% when RIP3 decreases

332   to 20% (Figure S5A). Whereas, the probability of BEC dynamics is decreased by 41.6% (Figure

333   5B). Thus, compared to biphasic, RIP3 seems to be more critical for the achievement of emergent

334   and coexistent dynamics.

335   To determine the regulation of RIP3 on the scale of biphasic dynamics H, 570 samples that

336   achieve BEC dynamics for 100% RIP3 are selected. The regulation of H by RIP3 has three types

337   and their corresponding proportions are calculated: negative regulation (H is decreased with RIP3

338   increases) with 16.49%, positive regulation (H is increased with RIP3 increases) with 54.74%, and

339   Bell-shaped regulation (nonlinear change in H with RIP3 increase) with 28.77% (Figure 5C). Three

340   specific systems are further selected to intuitively show how RIP3 negatively, positively, or

341   nonlinearly regulates H (Figure 5D, upper and middle panels). Another specific system is also

342   selected to present the death mode transitions from apoptosis to the coexistence of apoptosis and

343   necroptosis, and finally to the exclusive necroptosis state with the increase of RIP1 (Figure 5D,

344   down panel).

345   Similar regulation of C8 on H is shown in Figure S5B, where the proportion of systems that

346   achieving Bell-shaped regulation of H by C8 is less than ~10% compared to the regulation of RIP3

347   on H (Figure 5C). Thus, variation of RIP3 seems to be more easily than C8 to achieve Bell-shaped

348   regulation on H, supporting the results in the deterministic system that H does not present Bell-

349   shaped response to C8 variation (Figure S1C). The average and variation of $pRIP3_{peak}$ with the

350   decrease of RIP3 or C8 in the 570 systems are calculated as well (Figure 5E). The average of relative

351   $pRIP3_{peak}$ is concentrated at a high level and the variation is quite small, revealing that the scale-

352   free feature of necroptosis emergence (Figure 3A) is an intrinsic topological property of the death

353   circuit.

354   The essential module for achieving BE and BEC dynamics are discussed with random circuit

355   analysis as well. The interaction terms are completely blocked one by one in the 50,000 random

356   samples, and the statistical probabilities are shown in Figure 5F. Only when any one of the terms

357   (k_5, k_7, or k_9) is removed, the probability tends to be 0, suggesting that the RIP1-RIP3-C8 incoherent

358   feedforward loop is the necessary module to generate BE and BEC dynamics (Figure 5F and Figure

359   S5C). Positive feedback loop is proven to be necessary for coexistent dynamics[39-41]. Unlike the

360   deterministic system (Figure 2C), blocking the positive feedback of RIP3 to RIP1 (k_3) cannot arrest

361   coexistent dynamics (Figure 5F). While the probability of BEC is significantly decreased compared

362   to BE with the blockage of RIP3 self-activation (k_3). The contributions of all the four positive

363   feedback loops within the death circuit are studied (Figure S5D), revealing that only the positive

364   feedback loop formed by k_3 or k_8 is efficient for achieving the high occurrence probability of

365   coexistent dynamics.

366   The regulation strategies of H by all the circuit interaction terms are separately calculated

367   (Figures 5F and S5E). Consistent with deterministic system analysis (Figure 3E), the Bell-shaped

368   regulation of H by the two feedforward terms of k_5 and k_7 are also statistically confirmed (Figure

369   5F). Moreover, RIP3 self-activation term k_8 can also present Bell-shaped regulation on H, which is

370   not observed in the deterministic system (Figure S2B). Thus, besides the positive feedback of RIP3

371   to RIP1 (Figures 5Gi and 2D), RIP3 self-activation forms another positive feedback for efficiently

372   achieving coexistent dynamics and the Bell-shaped regulation on necroptosis biphasic dynamics

373   (Figure 5Gii). The RIP1-RIP3-C8 incoherent feedforward loop embedded with these two positive

374   feedback loops forms the fundamental hypermotif for robustly achieving BEC dynamics in the

375   death circuit (Figure 5G).

376
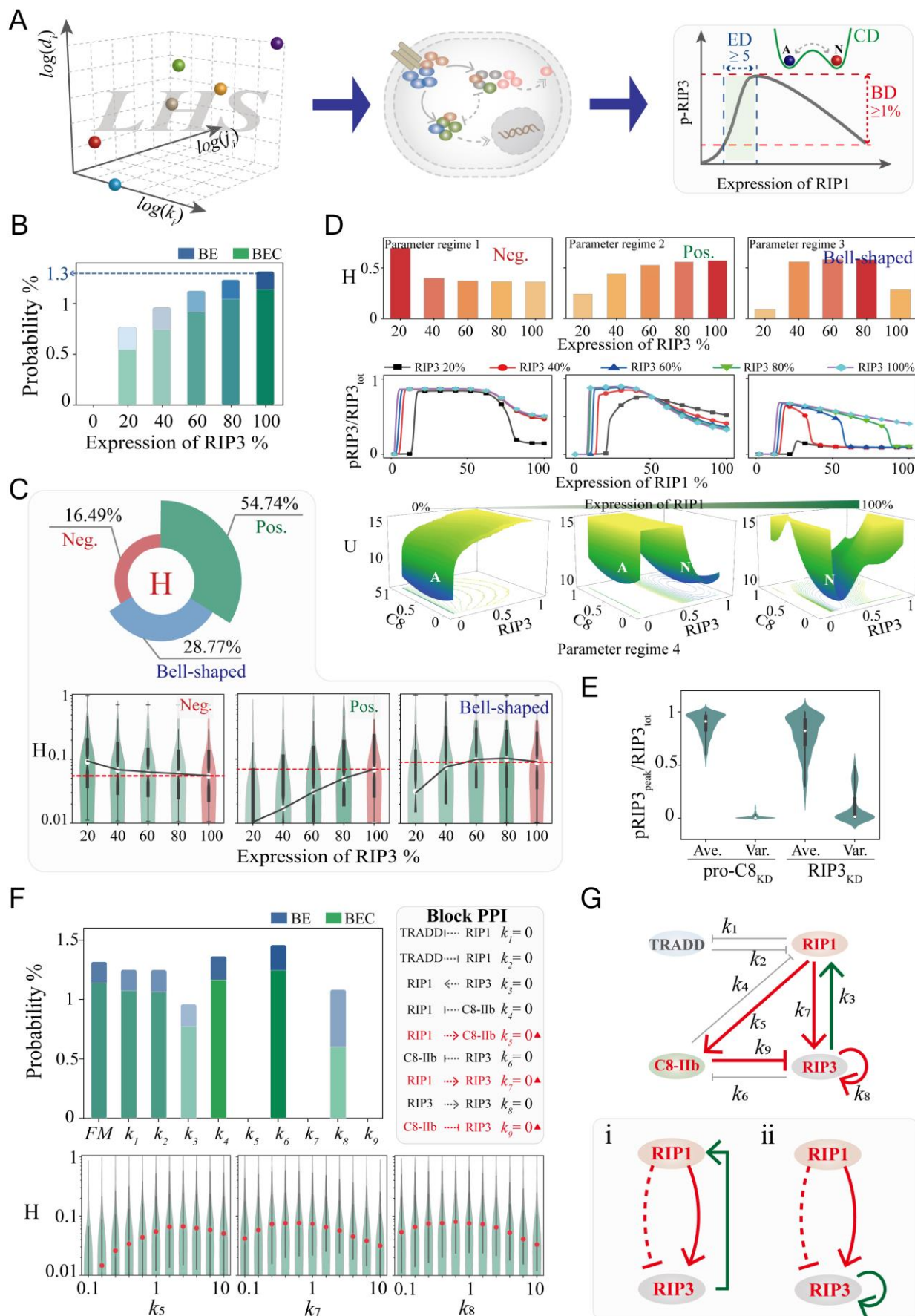
Figure 5. Identifying the core structure for necroptosis BEC dynamics with random circuit analysis. (A) Schematic of a computational workflow. Left panel: Latin hypercube sampling to obtain random parameter regimes. Right panel: Threshold settings for screened RIP1-dependent pRIP3 dynamics, including biphasic, emergent, and coexistent dynamics (BD, ED, and CD). (B) Random circuit analysis is used to search 50,000 systems under five representative RIP3 expression levels and count the probabilities that pRIP3 dynamic behaviors satisfy the threshold condition of BE and BEC dynamics. The blue and green histograms represent the probability of BE and BEC dynamics, respectively. (C) Statistics of the regulatory behavior of RIP3 on H in the screened systems with BEC dynamics. (D) Four representative systems of three different regulations of RIP3 on H (parameter regimes 1-3) and RIP1-dependent death modes switching behavior (parameter regimes 4). (E) The average and variance statistics of pRIP3peak relative level of all the screened samples with different expression levels of RIP3 and C8. (F) The probabilities of the system achieving BE (blue histograms) and BEC dynamics (green histograms) when any one term is removed. The terms of k_5, k_7, and k_9 (marked by red triangles) are individually removed and the system cannot achieve biphasic dynamics. Down panels: Statistics of terms strength on H in the screened systems. (G) The components and reactions in the death circuit to achieve BEC dynamics. Red lines indicate the necessary interaction of the incoherent feedforward loop. Green lines indicate the positive feedback to RIP3.

Topological exhaustivity defines three minimal circuits to achieve natural BE dynamics

To dissect the hidden design principles in biological systems, we tried to find the minimal circuit that performs biphasic dynamics with emergence. Topological exhaustive method has been widely used to explore the design of functional achievement in biological networks[4,16,42-44]. The workflow for circuit topology to function mapping of BE dynamics is shown in Figure S6A, which presents the circuit model described by coupling matrices, parameter regimes, and ordinary differential

402   equations. We first examined whether the output signal node in the two-node circuit could achieve

403   BE dynamics by the variation of the receiving node of input. All the 27 different structures of two-

404   node circuit are respectively assigned 100,000 sets of random parameter regimes, but none of these

405   circuits can achieve BE dynamics (Figure S6B).

406   We next searched BE dynamics in the three-node circuit, which includes an input node (node-

407   A), an output node (node-C), and a regulatory node (node-B) (Figure 6A). There are three types of

408   term (promotion, inhibition, and no interaction) between any two nodes. To map out the entire

409   design space of three-node circuits capable of BE dynamics, all the 4,698 circuits are exhausted

410   and analyzed with 50,000 sets of random parameter regimes assigned to each circuit. A total of

411   234.9 million dynamical systems (4,698×50,000 parameter regimes) are analyzed and finally 1,701

412   circuits that can achieve BE dynamics are screened out. To quantify the volume of the parameter

413   space in which circuit supports BE dynamics, the 4,698 coupling matrices are firstly reduced to

414   two-dimensional space using t-SNE method[45], and then the probabilities are converted into

415   topological potentials through -ln(p) analogy to the Boltzmann relation (Figure 6B). As a result, the

416   three potential wells in the topological landscape correspond to three sub-clusters respectively. The

417   three minimal circuits (M1, M2, and M3) in each sub-cluster are shown in Figure 6C, indicating

418   that the circuits have the common feature of containing incoherent feedforward loop. Similar results

419   are obtained with clustering analysis using the pair-wise distance between circuits, which also

420   divides the 1,701 circuits into three sub-clusters and finally refers to the same three minimal circuits

421   (Figure S7A).

422   Then, we severally segmented the obtained probabilities of the three sub-clusters into the two-

423   dimensional space of biphasic and emergent dynamics (Figure 6D). Probability distributions of the

424   three sub-clusters are quite different in the scale space. The sub-cluster of M1 circuit has a high

425   probability occurrence with a large scale of biphasic dynamics but with a low scale of emergent

426   dynamics (red square). While the sub-cluster of M2 circuit prefers to achieve a middle scale of

427 biphasic dynamics but with a small or high scale of emergent dynamics (red and orange squares).

428 M3 circuit sub-cluster is concentrated on attaining a small scale of biphasic dynamics, but with a

429 high scale of emergent dynamics (red square). Therefore, despite containing the incoherent

430 feedforward loop, the three minimal circuits exhibit divergence scales for achieving BE dynamics,

431 providing potential diversity control strategies in regulating various biological functions.

432 Starting from the three minimal circuits, the 1,701 circuits that can achieve BE dynamics are

433 generated by adding edges one by one. As a result, a comprehensive atlas describing the topological

434 evolution of three-node circuits and their corresponding probabilities for achieving BE dynamics

435 are entirely presented in Figure 6E. The topological complexity (the number of interaction

436 terms/edges E) of the atlas increases from bottom to top, and the probability of a circuit of the same

437 complexity to achieve BE dynamics decreases from left to right. The connectivity in the global atlas

438 of topological evolution could supervise any one interaction to enhance or resist the circuit

439 fulfillment function.

440 If an added edge improves the probability for achieving BE dynamics of the minimal circuit,

441 such an edge is functionally significant[38,46]. The statistical result of stochastically adding edges to

442 improve the probability of achieving BE dynamics based on the minimum motif M1 is shown in

443 Figure 6F. The result indicates that adding the self-activation of node C significantly increases the

444 probability for inducing BE dynamics. The probability is decreased by adding inhibition, but is

445 increased through considering the promotion of node C on node A. Based on the structure of adding

446 node C self-activation and the promotion of node C on node A, the probability reaches the highest

447 while further considering the inhibition of node B on node A and self-inhibition of node B in M1.

448 Positive feedback loop is proved to play decisive roles for realizing multi-stable states in biological

449 systems[39-41]. To discuss the structure of M1 for robustly achieving coexistent dynamics, six terms

450 which could form positive feedback loops in motif M1, are individually (diagonal node) or

451 integratively (non-diagonal node) added (Figure 6G). The proportion of the system with BEC

452 dynamics based on the achieved BE dynamics system is calculated, showing that the contribution

453 of node C self-activation is significant, and the proportion of system with coexistent dynamics is

454 the highest when the promotion of node C on node-A is added.

455   Taken together, for robustly achieving BEC dynamics, the structure shown in Figure 6H

456 should be the optimal circuit topology for M1, where red lines represent the essential edges while

457 blue lines are the regulatory edges. Actually, the experimentally determined RIP1-RIP3-C8 circuit

458 (Figure 1B) is highly consistent with the screened optimal circuit, revealing the precise design

459 strategy of the biological system in controlling cell death. The optimal structure for circuits M2 and

460 M3 are also discussed and the corresponding results are shown in Figures S7B and S7C.
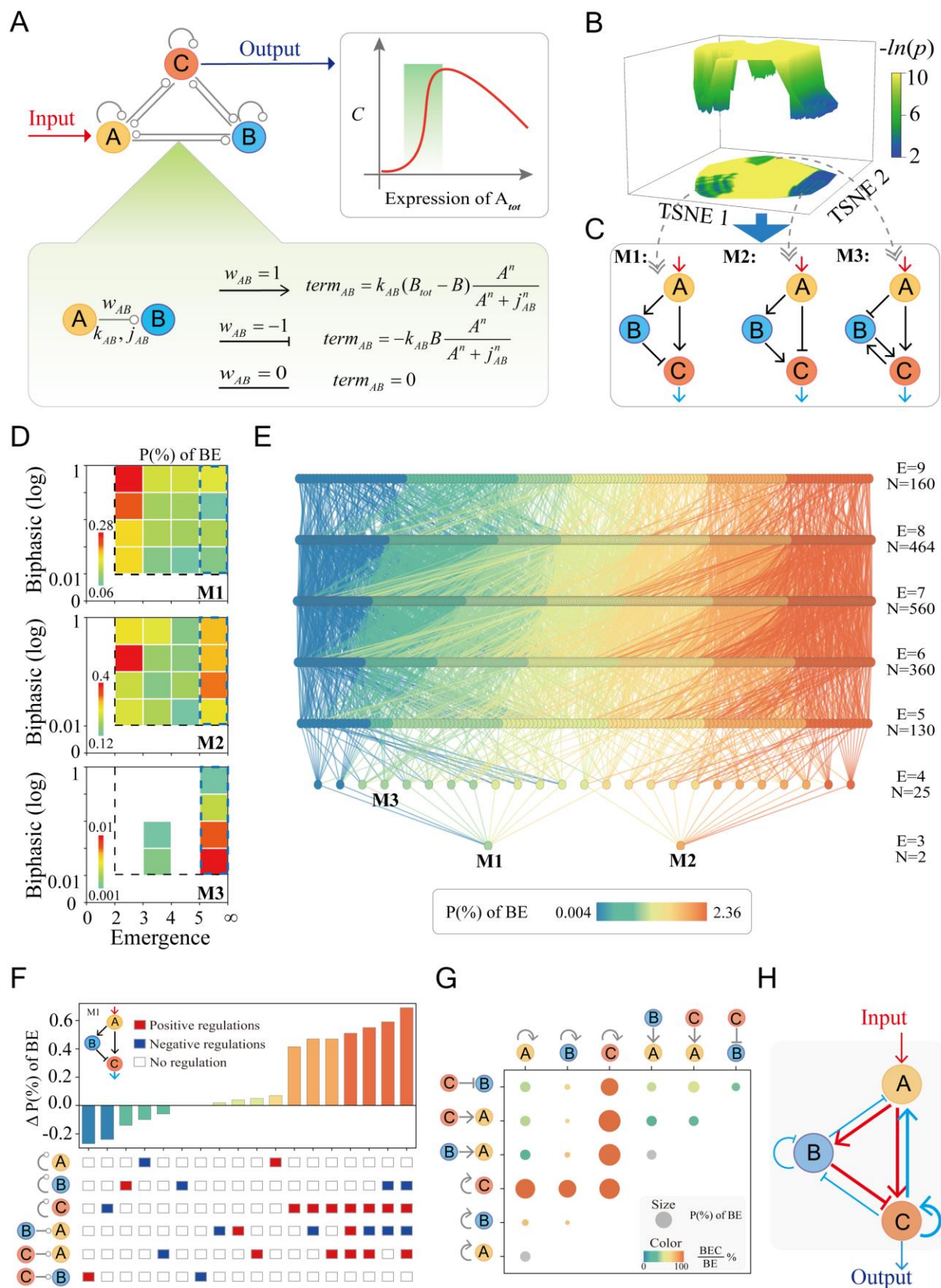
462 **Figure 6. Topological exhaustive method reveals a complete atlas of achieving BE dynamics**

463 **in three-node circuit.** (A) Illustration of the structure screening procedure from mapping topology

464 to function of asymmetric directed three-node circuit. A, B and C are the input node, regulatory

465 node, and output node, respectively. There are three kinds of edges between any two nodes, $w = 1$

466 means promotion, $w = -1$ means inhibition, and $w = 0$ means no interaction. (B) Topological

467 landscape of 4,698 coupling matrices in a 2D topological space. The well depth represents the

468 probability of a sub-cluster achieving BE dynamics. (C) The minimal circuit of the sub-clusters that

469 corresponds to the three wells in the topological landscape. (D) Probability distributions of the three

470 minimum circuits are mapped into the biphasic dynamics and emergence 2D scale spaces. (E) A

471 global atlas of 1,701 circuits that enable topological evolution of three-node circuits for achieving

472 BE dynamics. (F) Probability statistics of BE dynamics that can be achieved by adding edges based

473 on circuit M1. (G) The proportions of systems that with BEC dynamics when the six positive

474 feedback edges are added to M1 individually (diagonal node) or in combination (non-diagonal

475 node). (H) The determined optimal circuit for robustly achieving BEC dynamics.

476

477 **Discussion**

478 Crosstalk between pathways is easy to understand, but why a given end-result is eventually reached

479 is often a puzzle. As a key molecule in TNF signaling, RIP1 is required for inducing necroptosis[47].

480 While the inhibitory function of RIP1 is also demonstrated in mouse genetic studies[48,49]. How RIP1

481 regulates dynamics of downstream substrates in determining specific cell death outcomes is a long-

482 standing question[50,51]. We previously quantified the RIP1-induced biphasic dynamics of

483 necroptosis and further deciphered the control mechanisms[12]. However, the complexity of the

484 system and large number of parameters involved in previous model limit the generalizability of

485 conclusions and obscure the underlying mechanisms. To determine the topology and regulatory

486 mechanism for necroptosis biphasic, emergent, and coexistent dynamics, we proposed a circuit cell

487 death model of the TNF signaling based on previous studies[12] and our experimental data (Figure 1).

488 RIP1-RIP3-C8 incoherent feedforward loop is determined for achieving biphasic dynamics with

489 emergence, while the positive feedback loop of RIP3 on RIP1 is required for death mode

490 coexistence (Figure 2D). Instead of exploring the mechanisms with specific models, random

491 parameter analysis of the TNF circuit is also performed, identifying that the incoherent feedforward

492 loop embedded with RIP3 self-activation is another effective structure for achieving BEC dynamics

493 (Figure 5G). We attempted to explore whether there exist general circuit design principles for

494 natural systems to execute BE dynamics by using the topological landscape (Figure 6B), bottom-

495 up, and topological evolution (Figure 6E) strategies. Both two- and three-node circuits are

496 systematically analyzed and only three minimal three-node circuits are identified finally,

497 confirming that the incoherent feedforward loop is the essential module for BE dynamics.

498
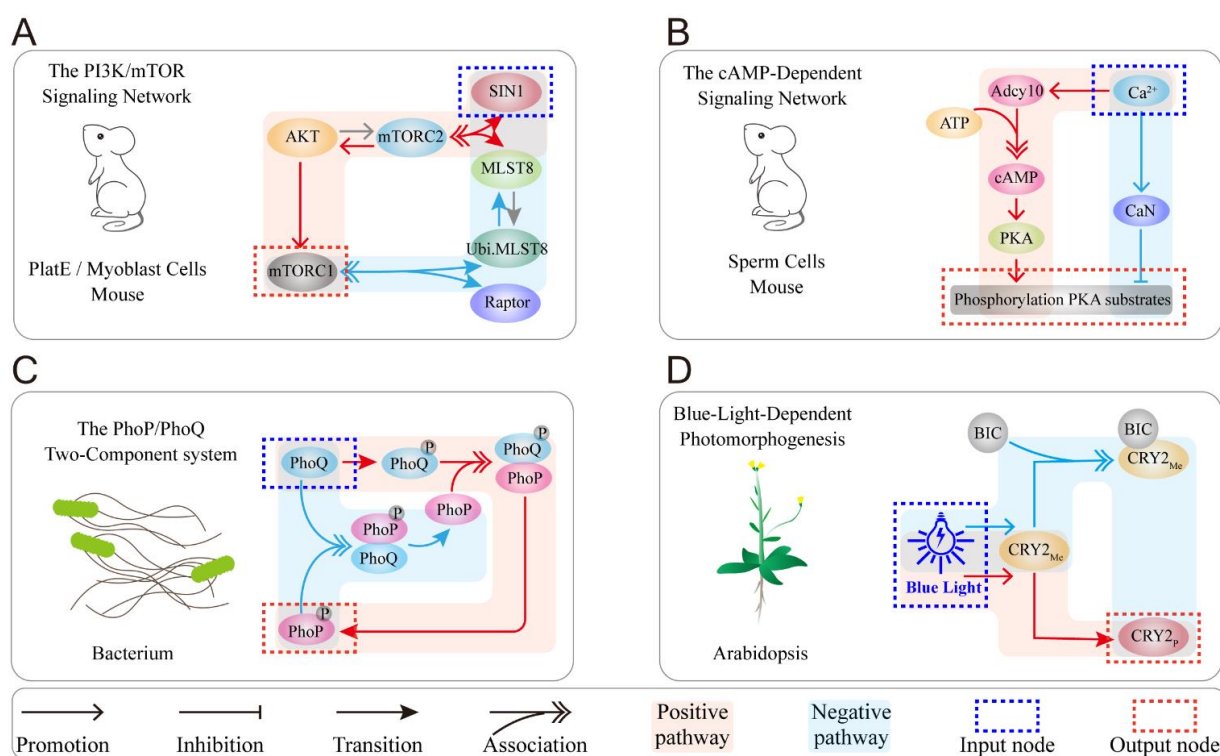
499

500 **Figure 7. Examples of biphasic dynamics induced by incoherent feedforward loop in various**

501 **cell types.** Blue backgrounds represent the negative regulatory pathway, and red backgrounds

502 represent the positive regulatory pathway. (A) Biphasic dependence of mTORC1 activity on SIN1

503   in mTOR signaling. (B) Biphasic function of calcium ions in cAMP-dependent signaling. (C) The

504   dual role of PhoQ in regulating PhoP phosphorylation in bacterial two-component system. (D)

505   Biphasic response of cryptochrome photoreceptor 2 (CRY2) to photomorphogenesis in Arabidopsis.

506

507   Biphasic dynamics have been observed to drive essential biological processes in all forms of

508   life, including mammalian cells, plant cells, and even bacterial cells. Previous study reported that

509   SIN1, a key mTORC2 subunit, biphasically regulates mTORC1 activity in Myoblast cells[52]. The

510   dynamics is determined by the incoherent feedforward loop shown in Figure 7A. Low-dose SIN1

511   promotes mTORC1 by synthesizing mTORC2, whereas high-dose SIN1 over-depletes MLST8

512   resulting in mTORC1 decreases. Biphasic dynamics is also observed in cAMP signaling which is

513   triggered by the incoherent feedforward loop[53] (Figure 7B). Calcium ions positively regulate

514   Adcy10 to promote cAMP synthesis and PKA activation in sperm flagellum, and also inhibit PKA

515   by activating CaN (calcineurin). Besides the mammalian cells, we previously found the biphasic

516   dynamics of PhoP phosphorylation regulated by PhoQ in bacteria[7]. The incoherent feedforward

517   loop exists in the PhoP/PhoQ signaling as well (Figure 7C). On the one hand, PhoQ promotes PhoP

518   phosphorylation through binding to PhoP. On the other hand, excess unphosphorylated PhoQ also

519   binds to phosphorylated PhoP to dephosphorylate PhoP. Our former study also observed the

520   biphasic dynamics of CRY2 controlled by blue light in Arabidopsis[9], and the incoherent feedback

521   loop is also hidden in the CRY2 signaling (Figure 7D). With the increase of light intensity, blue

522   light not only promotes the transition of $CRY2_{Me}$ to $CRY2_p$, but also promotes the combination of

523     $CRY2_{Me}$ and BIC to form a complex to reduce the level of $CRY2_p$. Taken together, the topology of

524   these signaling networks suggests that our determined incoherent feedforward loop should be a

525   generalizable design principle for robustly executing biphasic dynamics in biological systems.

526   Despite the complexity and diversity of cell signaling networks, their core module and central

527   topology should be highly conserved. Understanding the general design principles to achieve

528 specific functions in diverse biological systems is significant. Forward searching all two- or three-

529 node circuits are effective to find essential structures for achieving functions such as adaptation,

530 noise-attenuation, robust oscillation, *etc.*[4,16,42]. The biological systems frequently exhibit muti-

531 functions at the same time. Unlike the previous studies that mainly focused on one or two biological

532 functions, we identified the topological structure that can achieve three general functions, *i.e.*,

533 biphasic, emergent, and coexistent dynamics in this work. Among the identified circuits, auxiliary

534 interaction on M1 motif that increase the probability of functional achievement are consistent with

535 the experimentally observed RIP1-C8-RIP3 structure (Figures 2D and 6C), suggesting that the

536 biological systems are naturally optimal structures. Of course, topological exhaustivity is also a

537 powerful approach for predicting interaction in biological systems that have not been

538 experimentally observed. In our analysis, the three identified circuits (M1, M2, and M3) seem to

539 exhibit divergence scales for achieving BE dynamics (Figure 6D). While the intrinsic differences

540 among these circuits are not captured. Further studies are still needed to systematically compare the

541 general principles of these incoherent feedforward loops in exerting biological functions.

542 Cell states correspond to the attractors of the dynamical system, while potential landscape

543 captures the dynamical principles of cell state transitions through providing a global

544 characterization and stability measurement[54-56]. Potential landscape allows the targeted exploration

545 of fundamental features and switching strategies of cell fate decision processes, and their

546 application deepens our understanding of biological functions. Most recently, a new cell-aging fate

547 induced by overexpression of the lysine deacetylase Sir2 was found by using this approach[57].

548 Besides, an unexpected observation of the lineage specifiers that can facilitate reprogramming and

549 replace reprogramming factors of a corresponding lineage-specifying potential, was successfully

550 clarified with landscape analysis as well[58]. Here, our study quantitatively provides the stochastic

551 dynamics, the global nature, and the kinetic transitions of the cell death signaling. This is the first

552 landscape discussion of necroptosis signaling to investigate the regulation of death mode switching.

553 We systematically explored how the system structure changes the volume of the valleys, potentially

554 helping to develop therapeutic strategies for death control. However, while employing the

555 landscape theory, it is still difficult to use Fokker-Planck equation to solve the evolution probability

556 of high-dimensional complex system. Although it has been proven effective to coarse-grain a high-

557 dimension system into a low-dimension[59], the curse of dimensionality exists objectively. Thus, deep

558 learning method, truncated moment equations, partial self-consistent mean field approximation, and

559 trajectory density should be developed and further considered in future study[59-62].

560   For living systems with nonequilibrium multi-stable states, the essence of state switching is

561 violating the principle of detailed balance that occurs at the cost of increasing entropy[63]. However,

562 the complexity and only partial accessibility of living systems severely limit the inference of crucial

563 thermodynamic quantities, like the entropy production. Previous studies mostly considered coarse-

564 graining as a mapping method to simplify the complex systems to the reduced Markov networks.

565 Recent studies also sought to measure the rate of entropy production by estimating the probabilities

566 of forward and reverse trajectories in sufficiently long time series data. These theoretical

567 explorations provided groundbreaking insights into understanding the central dogma, cells sense

568 through receptors, and so on[37,64-66]. In this study, Shannon entropy is introduced for the first time

569 to measure the uncertainty of cell death mode transition. Information entropy presents a possible

570 paradigm for understanding the transformation of energy and information in cells to perform fate

571 decisions, and further consideration of the relationship between the information cost and the free

572 energy cost of nonequilibrium systems is also urgently needed. These analyses will provide novel

573 insights into the role of 'Maxwell's demon' in fate decisions in living systems[67,68]. However, due to

574 the macroscopic limitation of complex living systems, our work assumes that the state transitions

575 on the observed degrees of freedom are equivalent to the state transitions of all degrees of freedom

576 of the system. We cannot determine whether there are other state transitions based on partial

577   observations. The inference of information and energy associations in living systems is still an

578   obvious and enormous challenge.

579

Methods

Cell line and cell culture

Mouse fibrosarcoma L929 were obtained from ATCC. RIP1 KO, RIP3 KO, L929, TRADD KO and Caspase-8 KO L929 cells were generated by TALEN or CRISPR/Cas9 methods. The knock-out cells were determined by sequencing of targeted loci and immunoblotting of the expression of respective proteins. All cells were maintained in Dulbecco's modified Eagle's medium (DMEM), supplemented with 10% fetal bovine serum, 2 mM L-glutamine, 100 IU penicillin, and 100 mg/ml streptomycin at 37°C in a humidified incubator containing 5% CO2. The target sites were designed as follows: RIP3: "CTAACATTCTGCTGGA"; RIP1: "AACCGCGCTGAGTGAGTTGG"; TRADD: "AAGATGGCAGCCGGTCAGAA"; Caspase-8: "GTGTTCAAATACATACGCCT". All lentiviral-shRNAs were constructed into pLV-H1-EF1α-puro vector or pLV-H1TetO-GFP-Bsd following the manufacturer's instruction (Biosettia). The indicated shRNA target sequences was: RIP1 shRNA: 5'-GCATTGTCCTTTGGGCAAT-3'.

Reagents and antibodies

Mouse TNF-α were obtained from eBioscience (San Diego, CA, USA). Anti-RIP3 (dilution 1:1,000) and anti-MLKL (dilution 1:1,000) were raised using E. coli-expressed GST-RIP3 (287-387 amino acid), GST-MLKL (100-200 amino acids) and GST-FADD (full length), respectively. Anti-caspase-8 antibody (4790, dilution 1:1000) and anti-cleaved caspase-8 antibody (8592, dilution 1:500) were purchased from Cell Signaling Technology. Anti-p-RIP3 antibody (ab222320, dilution 1:500) and anti-p-MLKL antibody (ab196436, dilution 1:1,000) were purchased from Abcam. Anti-Gapdh antibody (60004-1-Ig, dilution 1:2,000) were from Proteintech. Anti-RIP1 antibody (610459, dilution 1:1,000) was from BD Biosciences.

Immunoprecipitation and western blotting

Cells were seeded in a 100 mm dish, grew to reach confluency. After stimulating, cells were washed by PBS for three times and then lysed with lysis buffer (20 mM Tris-HCl, pH 7.5, 150 mM NaCl, 1 mM Na2EDTA, 1 mM EGTA, 1% Triton X-100, 2.5 mM sodium pyrophosphate, 1 mM β-glycerophosphate, 1 mM Na3VO4) on ice for 30 min. Cell lysates were then centrifuged at 20,000 g for 30 min. The supernatant was immunoprecipitated with anti-Flag M2 beads at 4°C overnight. After the immunoprecipitation, the beads were washed three times in lysis buffer and the immunoprecipitated proteins were subsequently eluted by SDS sample buffer with 0.15 µg/µL 3×Flag peptide.

Microscopy imaging of cell death

To examine cell death morphology, cells were treated as indicated in 12-well plates or 35-mm glass bottom dishes for image capture. Static bright-field images of cells were captured using Zeiss LSM 780 at room temperature. The pictures were processed using Image J or the ZEN 2012 Image program.

Noise and potential landscape

There is randomness in the procedure of biochemical reactions in cells, including intrinsic randomness, that is, molecular noise, and thermal fluctuations in the biochemical environment[69,70]. For simplicity, we add a noise term, $\sigma d\xi$, to the OEDs of the deterministic model and assume that the noise intensity is correlated with the protein level. ξ represents for white Gaussian noise, and the statistical properties satisfy $<\xi_i(t)> = 0$ and $<\xi_i(t)\,\xi_i(t')> = 2\sigma\delta(t-t')$.

The global dynamics of a stochastic system with noise are given by the potential landscape. The stochastic dynamics of cell death fate decision system could be characterized by the generalized Langevin equation $dx_i(t)/dt = F(x_i) + \xi(t)$, where x represents the concentrations of the proteins and

630   F is the driving force. The Fokker-Planck equation describes the evolution of the probability density

631   p in the state space, as following: $\partial p(x_i, t)/\partial t = -\Sigma\partial(F(x_i)\,p(x_i, t))/\partial x_i + D_i\Sigma\partial^2 p(x_i, t)/\partial x_i^2$. Since the

632   dimensionality of the model limits the direct access to the probability density through the evolution

633   of the Fokker–Planck equation. We use the Bernoulli experiment numerical method to replace the

634   steady-state probability distribution with the trajectory density distribution in the phase space.

635   Specifically, we divide the two-dimensional phase space of RIP3 and C8 into 200×200 lattices and

636   assign 10,000 sets of random initial conditions to the stochastic differential equations. After a long

637   enough evolution, 10,000 trajectories can be obtained in the phase space, and the number of

638   trajectories in each lattice is counted and the density is calculated[58].

639

Identification of biphasic dynamics with emergence

641   In this study, the system depends on normalized TNF stimulation to be activated, the strength

642   of which is a random value in the range (0,1]. The levels of C8 and pRIP3 are also dependent on

643   the upstream signaling molecule RIP1, and the knockdown of RIP1 means that the signal could not

644   be transmitted to downstream signaling molecules. In numerical simulations, the scale H of the

645   biphasic kinetics is dependent on the peak pRIP3 level and the level when RIP1 is not knocked

646   down (deterministic model). The expression of RIP1 is fixed as a control parameter, discretized

647   with a step size of 0.02 in the normalized parameter space. First, a two-dimensional array of RIP1-

648   dependent pRIP3 level and an index of RIP1 expression corresponding to pRIP3 peak are obtained

649   through time evolution. Second, the elements in the two-dimensional array must satisfy the

650   characteristics of monotonically increasing on the left of indexpRIP3peak and decreasing

651   monotonically on the right. Finally, the pRIP3 level at 100% RIP1 expression must be 0.01 lower

652   than the *pRIP3$_{peak}$*. The emergent behavior should satisfy the level of pRIP3 increased by not less

653   than 50% when RIP1 expression continuously increases by 10%.

654

Explanation of topological exhaustive method

Here we seek to uncover the minimal core motifs that enable biological networks to achieve biphasic and emergent kinetics. The study of functional motifs in complex biological networks based on node directed networks has been widely reported[4,38,42], and thus is also applicable to the achievement of biphasic and emergent kinetics for more complex biological networks embedded with the minimal core motifs we found.

For the two-node directed network, each topology corresponds to a 2×2 coupling matrix, and each coupling edge could be assigned to 1 (promoting), -1 (inhibiting), and 0 (no interaction). There are theoretically 3^4 (=81) topologies. However, the heterogeneity of input and output nodes was considered in this study, the activation of the output node depends on the input node, and the control parameter is fixed to the protein (gene) expression amount represented by the input node. Therefore, the coupling edge of the input node to the output node can only be fixed to 1, and finally only 27 topologies are considered. For a three-node directed network, a control node is introduced, and the system also relies on the activation of input nodes. The constraints of interaction include 1) the output node must have a promoting action from the input node or regulatory node; 2) the regulatory node must have a promoting action from the input node or output node; 3) one of the input nodes and output nodes must be promoted or inhibited by the regulated node. A class of motifs is eliminated from all motifs that meet the above three conditions, and their output node and regulatory node promote each other but are not promoted by the input node. The theoretical 3^9 (=16983) topologies are reduced to 4,698.

Parameter ranges selection and sampling

In our study, the parameter ranges of the computational models were consistent with those in previous publications of similar studies[4,38,71]. For each topology, 50,000 parameter sets are uniformly sampled using Latin hypercube sampling, with parameters ranging from k~0.1-10

680 (logarithmic scale), j~0.001-100(logarithmic scale), d~0.01-1(logarithmic scale), n~1-4(integer

681 scale), stimulation signal~0-1.

682

Data availability

684 The data of this work are available from the corresponding author upon reasonable request.

685

Code availability

687 The key codes for this work are deposited to GitHub at https://github.com/XMU-Xu/ANscn.

688 Other reasonable requirements can be obtained from the corresponding author.

689

REFERENCES

1   Nagashima, T. *et al.* Quantitative transcriptional control of ErbB receptor signaling undergoes graded to biphasic response for cell differentiation. *Journal of Biological Chemistry* **282**, 4045-4056, doi:10.1074/jbc.M608653200 (2007).

2   Shin, D. *et al.* The hidden switches underlying ROR alpha-mediated circuits that critically regulate uncontrolled cell proliferation. *Journal of Molecular Cell Biology* **6**, 338-348, doi:10.1093/jmcb/mju023 (2014).

3   Shin, S. Y. *et al.* The switching role of beta-adrenergic receptor signalling in cell survival or death decision of cardiomyocytes. *Nature Communications* **5**, doi:10.1038/ncomms6777 (2014).

4   Ma, W. Z., Trusina, A., El-Samad, H., Lim, W. A. & Tang, C. Defining Network Topologies that Can Achieve Biochemical Adaptation. *Cell* **138**, 760-773, doi:10.1016/j.cell.2009.06.013 (2009).

5   Basu, S., Mehreja, R., Thiberge, S., Chen, M. T. & Weiss, R. Spatiotemporal control of gene expression with pulse-generating networks. *Proceedings of the National Academy of Sciences of the United States of America* **101**, 6355-6360, doi:10.1073/pnas.0307571101 (2004).

6   Sasagawa, S., Ozaki, Y., Fujita, K. & Kuroda, S. Prediction and validation of the distinct dynamics of transient and sustained ERK activation. *Nature Cell Biology* **7**, 365-U331, doi:10.1038/ncb1233 (2005).

7   Liu, W. *et al.* Biphasic regulation of transcriptional surge generated by the gene feedback loop in a two-component system. *Bioinformatics* **37**, 2682-2690, doi:10.1093/bioinformatics/btab138 (2021).

8   Tamotsu, S., Schomerus, C., Stehle, J. H., Roseboom, P. H. & Korf, H. W. NOREPINEPHRINE-INDUCED PHOSPHORYLATION OF THE TRANSCRIPTION

FACTOR CREB IN ISOLATED RAT PINEALOCYTES - AN IMMUNOCYTOCHEMICAL STUDY. *Cell and Tissue Research* **282**, 219-226, doi:10.1007/bf00319113 (1995).

9   Wu, Y. N. *et al.* Different response modes and cooperation modulations of blue-light receptors in photomorphogenesis. *Plant Cell and Environment* **44**, 1802-1815, doi:10.1111/pce.14038 (2021).

10   Xu, F., Zhang, J. Q., Jin, M., Huang, S. F. & Fang, T. T. Chimera states and synchronization behavior in multilayer memristive neural networks. *Nonlinear Dynamics* **94**, 775-783, doi:10.1007/s11071-018-4393-9 (2018).

11   Xu, F., Zhang, J. Q., Fang, T. T., Huang, S. F. & Wang, M. S. Synchronous dynamics in neural system coupled with memristive synapse. *Nonlinear Dynamics* **92**, 1395-1402, doi:10.1007/s11071-018-4134-0 (2018).

12   Li, X. *et al.* RIP1-dependent linear and nonlinear recruitments of caspase-8 and RIP3 respectively to necrosome specify distinct cell death outcomes. *Protein & Cell* **12**, 858-876, doi:10.1007/s13238-020-00810-x (2021).

13   Newman, M. E. J. & Clauset, A. Structure and inference in annotated networks. *Nature Communications* **7**, doi:10.1038/ncomms11863 (2016).

14   Lambiotte, R., Rosvall, M. & Scholtes, I. From networks to optimal higher-order models of complex systems. *Nat. Phys.* **15**, 313-320, doi:10.1038/s41567-019-0459-y (2019).

15   Sanchez-Garcia, R. J. Exploiting symmetry in network analysis. *Communications Physics* **3**, doi:10.1038/s42005-020-0345-z (2020).

16   Li, Z. D., Liu, S. X. & Yang, Q. Incoherent Inputs Enhance the Robustness of Biological Oscillators. *Cell Syst.* **5**, 72-81, doi:10.1016/j.cels.2017.06.013 (2017).

738   17   Qiao, L., Zhang, Z.-B., Zhao, W., Wei, P. & Zhang, L. Network design principle for robust

739   oscillatory behaviors with respect to biological noise. *eLife* **11**, doi:10.7554/eLife.76188

740   (2022).

741   18   Broido, A. D. & Clauset, A. Scale-free networks are rare. *Nature Communications* **10**,

742   doi:10.1038/s41467-019-08746-5 (2019).

743   19   Chen, X. *et al.* Mosaic composition of RIP1-RIP3 signalling hub and its role in regulating

744   cell death. *Nature Cell Biology* **24**, 471-+, doi:10.1038/s41556-022-00854-7 (2022).

745   20   Wang, L., Du, F. H. & Wang, X. D. TNF-alpha induces two distinct caspase-8 activation

746   pathways. *Cell* **133**, 693-703, doi:10.1016/j.cell.2008.03.036 (2008).

747   21   Zhang, D. W. *et al.* RIP3, an Energy Metabolism Regulator That Switches TNF-Induced

748   Cell   Death   from   Apoptosis   to   Necrosis.   *Science*   **325**,   332-336,

749   doi:10.1126/science.1172308 (2009).

750   22   Brenner, D., Blaser, H. & Mak, T. W. Regulation of tumour necrosis factor signalling: live

751   or let die. *Nature Reviews Immunology* **15**, 362-374, doi:10.1038/nri3834 (2015).

752   23   Han, J. H., Zhong, C. Q. & Zhang, D. W. Programmed necrosis: backup to and competitor

753   with   apoptosis   in   the   immune   system.   *Nature   Immunology*   **12**,   1143-1149,

754   doi:10.1038/ni.2159 (2011).

755   24   Zheng, L. X. *et al.* Competitive control of independent programs of tumor necrosis factor

756   receptor-induced cell death by TRADD and RIP1. *Molecular and Cellular Biology* **26**,

757   3505-3513, doi:10.1128/mcb.26.9.3505-3513.2006 (2006).

758   25   Nunez, R., Sancho-Martinez, S. M., Novoa, J. M. L. & Lopez-Hernandez, F. J. Apoptotic

759   volume decrease as a geometric determinant for cell dismantling into apoptotic bodies. *Cell*

760   *Death and Differentiation* **17**, 1665-1671, doi:10.1038/cdd.2010.96 (2010).

26   Orozco, S. *et al.* RIPK1 both positively and negatively regulates RIPK3 oligomerization and necroptosis. *Cell Death and Differentiation* **21**, 1511-1521, doi:10.1038/cdd.2014.76 (2014).

27   Oberst, A. *et al.* Catalytic activity of the caspase-8-FLIPL complex inhibits RIPK3-dependent necrosis. *Nature* **471**, 363-367, doi:10.1038/nature09852 (2011).

28   Yang, Z. H. *et al.* A Non-canonical PDK1-RSK Signal Diminishes Pro-caspase-8-Mediated Necroptosis Blockade. *Molecular Cell* **80**, 296-310, doi:10.1016/j.molcel.2020.09.004 (2020).

29   Li, J. X. *et al.* The RIP1/RIP3 Necrosome Forms a Functional Amyloid Signaling Complex Required for Programmed Necrosis. *Cell* **150**, 339-350, doi:10.1016/j.cell.2012.06.019 (2012).

30   Mompean, M. *et al.* The Structure of the Necrosome RIPK1-RIPK3 Core, a Human Hetero-Amyloid Signaling Complex. *Cell* **173**, 1244-1253, doi:10.1016/j.cell.2018.03.032 (2018).

31   Fang, X. N., Kruse, K., Lu, T. & Wang, J. Nonequilibrium physics in biology. *Reviews of Modern Physics* **91**, doi:10.1103/RevModPhys.91.045004 (2019).

32   Wang, J., Xu, L. & Wang, E. K. Potential landscape and flux framework of nonequilibrium networks: Robustness, dissipation, and coherence of biochemical oscillations. *Proceedings of the National Academy of Sciences of the United States of America* **105**, 12271-12276, doi:10.1073/pnas.0800579105 (2008).

33   Chu, X. K. & Wang, J. Quantifying Chromosome Structural Reorganizations During Differentiation, Reprogramming, and Transdifferentiation. *Physical Review Letters* **129**, doi:10.1103/PhysRevLett.129.068102 (2022).

34   Skinner, D. J. & Dunkel, J. Estimating Entropy Production from Waiting Time Distributions. *Physical Review Letters* **127**, doi:10.1103/PhysRevLett.127.198101 (2021).

785   35   Skinner, D. J. & Dunkel, J. Improved bounds on entropy production in living systems. *Proceedings of the National Academy of Sciences of the United States of America* **118**, doi:10.1073/pnas.2024300118 (2021).

788   36   Neri, I., Roldan, E. & Julicher, F. Statistics of Infima and Stopping Times of Entropy Production and Applications to Active Molecular Processes. *Phys. Rev. X* **7**, doi:10.1103/PhysRevX.7.011019 (2017).

791   37   van der Meer, J., Ertel, B. & Seifert, U. Thermodynamic Inference in Partially Accessible Markov Networks: A Unifying Perspective from Transition-Based Waiting Time Distributions. *Phys. Rev. X* **12**, doi:10.1103/PhysRevX.12.031025 (2022).

794   38   Xu, F. *et al.* Oscillations Governed by the Incoherent Dynamics in Necroptotic Signaling. *Front. Physics* **9**, doi:10.3389/fphy.2021.726638 (2021).

796   39   Chang, D. E. *et al.* Building biological memory by linking positive feedback loops. *Proceedings of the National Academy of Sciences of the United States of America* **107**, 175-180, doi:10.1073/pnas.0908314107 (2010).

799   40   Otero-Muras, I., Yordanov, P. & Stelling, J. Chemical Reaction Network Theory elucidates sources of multistability in interferon signaling. *PLoS Comput. Biol.* **13**, doi:10.1371/journal.pcbi.1005454 (2017).

802   41   Freyer, F., Roberts, J. A., Ritter, P. & Breakspear, M. A Canonical Model of Multistability and Scale-Invariance in Biological Systems. *PLoS Comput. Biol.* **8**, doi:10.1371/journal.pcbi.1002634 (2012).

805   42   Qiao, L. X., Zhao, W., Tang, C., Nie, Q. & Zhang, L. Network Topologies That Can Achieve Dual Function of Adaptation and Noise Attenuation. *Cell Syst.* **9**, 271-285, doi:10.1016/j.cels.2019.08.006 (2019).

808   43   Huang, B. *et al.* Interrogating the topological robustness of gene regulatory circuits by randomization. *PLoS Comput. Biol.* **13**, doi:10.1371/journal.pcbi.1005456 (2017).

810 44 Adler, M., Szekely, P., Mayo, A. & Alon, U. Optimal Regulatory Circuit Topologies for

811   Fold-Change Detection. *Cell Syst.* **4**, 171-181, doi:10.1016/j.cels.2016.12.009 (2017).

812 45 van der Maaten, L. & Hinton, G. Visualizing Data using t-SNE. *Journal of Machine*

813   *Learning Research* **9**, 2579-2605 (2008).

814 46 Jolley, C. C., Ode, K. L. & Ueda, H. R. A Design Principle for a Posttranslational

815   Biochemical Oscillator. *Cell Reports* **2**, 938-950, doi:10.1016/j.celrep.2012.09.006 (2012).

816 47 Cho, Y. *et al.* Phosphorylation-Driven Assembly of the RIP1-RIP3 Complex Regulates

817   Programmed Necrosis and Virus-Induced Inflammation. *Cell* **137**, 1112-1123,

818   doi:10.1016/j.cell.2009.05.037 (2009).

819 48 Dillon, C. P. *et al.* RIPK1 Blocks Early Postnatal Lethality Mediated by Caspase-8 and

820   RIPK3. *Cell* **157**, 1189-1202, doi:10.1016/j.cell.2014.04.018 (2014).

821 49 Newton, K. *et al.* RIPK1 inhibits ZBP1-driven necroptosis during development. *Nature* **540**,

822   129-133, doi:10.1038/nature20559 (2016).

823 50 Green, D. R. Another face of RIPK1. *Embo Reports* **16**, 674-675,

824   doi:10.15252/embr.201540470 (2015).

825 51 Weinlich, R. & Green, D. R. The Two Faces of Receptor Interacting Protein Kinase-1.

826   *Molecular Cell* **56**, 469-480, doi:10.1016/j.molcel.2014.11.001 (2014).

827 52 Ghomlaghi, M., Yang, G., Shin, S., James, D. E. & Nguyen, L. K. Dynamic modelling of

828   the PI3K/MTOR signalling network uncovers biphasic dependence of mTORC1 activity on

829   the mTORC2 subunit SIN1. *PLoS Comput. Biol.* **17**, doi:10.1371/journal.pcbi.1008513

830   (2021).

831 53 Navarrete, F. A. *et al.* Biphasic Role of Calcium in Mouse Sperm Capacitation Signaling

832   Pathways. *Journal of Cellular Physiology* **230**, 1758-1769, doi:10.1002/jcp.24873 (2015).

833   54   Saez, M. *et al.* Statistically derived geometrical landscapes capture principles of decision-making dynamics during cell fate transitions. *Cell Syst.* **13**, 12-28.e13, doi:10.1016/j.cels.2021.08.013 (2022).

836   55   Zhu, L. G. *et al.* Network modeling-based identification of the switching targets between pyroptosis and secondary pyroptosis. *Chaos Solitons & Fractals* **155**, doi:10.1016/j.chaos.2021.111724 (2022).

839   56   Li, X. *et al.* Caspase-1 and Gasdermin D Afford the Optimal Targets with Distinct Switching Strategies in NLRP1b Inflammasome-Induced Cell Death. *Research* **2022**, doi:10.34133/2022/9838341 (2022).

842   57   Li, Y. *et al.* A programmable fate decision landscape underlies single-cell aging in yeast. *Science* **369**, 325-329, doi:10.1126/science.aax9552 (2020).

844   58   Shu, J. *et al.* Induction of Pluripotency in Mouse Somatic Cells with Lineage Specifiers. *Cell* **153**, 963-975, doi:10.1016/j.cell.2013.05.001 (2013).

846   59   Kang, X. & Li, C. H. A Dimension Reduction Approach for Energy Landscape: Identifying Intermediate States in Metabolism-EMT Network. *Advanced Science* **8**, doi:10.1002/advs.202003133 (2021).

849   60   Kang, X., Wang, J. & Li, C. H. Exposing the Underlying Relationship of Cancer Metastasis to Metabolism and Epithelial-Mesenchymal Transitions. *Iscience* **21**, 754-772, doi:10.1016/j.isci.2019.10.060 (2019).

852   61   Zhang, J. *et al.* Deep Representation Learning for Complex Free-Energy Landscapes. *Journal of Physical Chemistry Letters* **10**, 5571-5576, doi:10.1021/acs.jpclett.9b02012 (2019).

855   62   Xu, Y. *et al.* Solving Fokker-Planck equation using deep learning. *Chaos* **30**, doi:10.1063/1.5132840 (2020).

857   63   Mehta, P. & Schwab, D. J. Energetic costs of cellular computation. *Proceedings of the*

858   *National Academy of Sciences of the United States of America* **109**, 17978-17982,

859   doi:10.1073/pnas.1207814109 (2012).

860   64   Barato, A. C. & Seifert, U. Thermodynamic Uncertainty Relation for Biomolecular

861   Processes. *Physical Review Letters* **114**, doi:10.1103/PhysRevLett.114.158101 (2015).

862   65   Lang, A. H., Fisher, C. K., Mora, T. & Mehta, P. Thermodynamics of Statistical Inference

863   by Cells. *Physical Review Letters* **113**, doi:10.1103/PhysRevLett.113.148103 (2014).

864   66   Still, S., Sivak, D. A., Bell, A. J. & Crooks, G. E. Thermodynamics of Prediction. *Physical*

865   *Review Letters* **109**, doi:10.1103/PhysRevLett.109.120604 (2012).

866   67   Dutta, S. Thermodynamics of multiple Maxwell demons. *European Physical Journal B* **95**,

867   doi:10.1140/epjb/s10051-022-00394-x (2022).

868   68   Ito, S. & Sagawa, T. Maxwell's demon in biochemical signal transduction with feedback

869   loop. *Nature Communications* **6**, doi:10.1038/ncomms8498 (2015).

870   69   Engberg, N., Kahn, M., Petersen, D. R., Hansson, M. & Serup, P. Retinoic Acid Synthesis

871   Promotes Development of Neural Progenitors from Mouse Embryonic Stem Cells by

872   Suppressing Endogenous, Wnt-Dependent Nodal Signaling. *Stem Cells* **28**, 1498-1509,

873   doi:10.1002/stem.479 (2010).

874   70   Eling, N., Morgan, M. D. & Marioni, J. C. Challenges in measuring and understanding

875   biological noise. *Nature Reviews Genetics* **20**, 536-548, doi:10.1038/s41576-019-0130-6

876   (2019).

877   71   Tsai, T. Y. C. *et al.* Robust, tunable biological oscillations from interlinked positive and

878   negative feedback loops. *Science* **321**, 126-129, doi:10.1126/science.1156951 (2008).

879   72   Li, Z. D., Liu, S. X. & Yang, Q. Incoherent Inputs Enhance the Robustness of Biological

880   Oscillators. *Cell Syst.* **5**, 72-+, doi:10.1016/j.cels.2017.06.013 (2017).

881

Acknowledgements

Author contributions

Fei Xu conceived the idea, developed the algorithms, analyzed the data and wrote the paper. Xiang Li conceived the idea, analyzed the data and wrote the paper. Rui Wu performed the experimental analysis. Hong Qi, Jun Jin, Zhilong Liu, Yuning Wu, Chuanshen Shen and Hai Lin helped to analyze data. Jianwei Shuai revised the paper and supervised the project. Fei Xu and Xiang Li contributed equally to this work.

Competing interests

All other authors declare they have no competing interests

907 Supplemental Information for:

908 **Topological design principle for the robustness of necroptosis biphasic, emergent, and**

909 **coexistent (BEC) dynamics**

910 **Fei Xu *et al.***

911

912 **Computational modeling**

913 Ordinary differential equations are built to describe the evolutionary dynamics of cell death

914 signaling mediated by TNF[71,72]. For example, the interaction of RIP3 phosphorylation by pRIP1 is:

915
$$[RIP3] + n[pRIP1] \underset{k_{OFF}}{\overset{k_{ON}}{\rightleftarrows}} [RIP3 \cdot pRIP1_n] \overset{k}{\rightarrow} [pRIP3] + n[pRIP1]$$
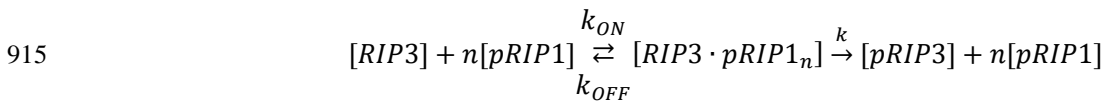
916 The equation of the intermediate complex [pRIP1·RIP3] is described as follows:

917
$$\frac{d[RIP3 \cdot pRIP1_n]}{dt} = k_{ON} * [RIP3] * [pRIP1]^n - k_{OFF} * [RIP3 \cdot pRIP1_n] - k * [RIP3 \cdot pRIP1_n]$$

918 At steady state,

919
$$[RIP3 \cdot pRIP1_n] = \frac{k_{ON}}{k_{OFF} + k} * [RIP3] * [pRIP1]^n$$

920 Assuming the binding between proteins is independent, and the dissociation rate of the complex is

921 much larger than the binding rate.

922
$$[RIP3 \cdot pRIP1_n] = [RIP3]_{tot} - [pRIP3] - [RIP3]$$

923 With the normalized total amount of proteins, the rate of pRIP1-mediated phosphorylation of pRIP3

924 is described as follows:

925
$$v_{pRIP3\ activated\ by\ pRIP1} = k * (1 - [pRIP3]) \frac{pRIP1^n}{pRIP1^n + \frac{k_{OFF} + k}{k_{ON}}} = k * (1 - [pRIP3]) \frac{[pRIP1]^n}{[pRIP1]^n + j^n}$$

926

927

928

929 The complete equations of deterministic TNF circuit model are presented below:

ODEs	Interaction term		Parameters
$\dfrac{d[acTRADD]}{dt} = F_{TRADD}$ $F_{TRADD} = v_1 - v_2 - v_3$	Activation by *TNF* $v_1 = k_{ac1} * (1 - [acTRADD]) * \dfrac{[TNF]^{n_{ac1}}}{([TNF]^{n_{ac1}} + j_{ac1}^{n_{ac1}})}$		k_{ac1}=1.7 j_{ac1}=0.012 n_{ac1}=3
	Inhibition by *pRIP1* $v_2 = k_1 * [acTRADD] * \dfrac{[pRIP1]^{n_1}}{([pRIP1]^{n_1} + j_1^{n_1})}$		k_1=9.5 j_1=0.12 n_1=2
	Degradation $v_3 = d_1 * [acTRADD]$		d_1=0.03
$\dfrac{d[pRIP1]}{dt} = F_{RIP1}$ $F_{RIP1} = v_4 + v_5 - v_6 - v_7$ $- v_8$	Activation by *TNF* $v_4 = k_{ac2} * (1 - [pRIP1]) * \dfrac{[TNF]^{n_{ac2}}}{([TNF]^{n_{ac2}} + j_{ac2}^{n_{ac2}})}$		k_{ac2}=0.35 j_{ac2}=2.3 n_{ac2}=1
	Phosphorylation by pRIP3 $v_5 = k_3 * (1 - [pRIP1]) * \dfrac{[pRIP3]^{n_3}}{([pRIP3]^{n_3} + j_3^{n_3})}$		k_3=6.7 j_3=1.2 n_3=3
	Inhibition by *acTRADD* $v_6 = k_2 * [pRIP1] * \dfrac{[acTRADD]^{n_2}}{([acTRADD]^{n_2} + j_2^{n_2})}$		k_2=0.17 j_2=1.47 n_2=4
	Cleavage by *C8* in Complex-IIb $v_7 = k_4 * [pRIP1] * \dfrac{[C8_{IIb}]^{n_4}}{([C8_{IIb}]^{n_4} + j_4^{n_4})}$		k_4=1.4 j_4=0.008 n_4=4
	Degradation $v_8 = d_2 * [pRIP1]$		d_2=0.1
$\dfrac{d[pRIP3]}{dt} = F_{RIP3}$ $F_{RIP3} = v_9 + v_{10} - v_{11} - v_{12}$	Phosphorylation by *pRIP1* $v_9 = k_7 * (1 - [pRIP3]) * \dfrac{[pRIP1]^{n_7}}{([pRIP1]^{n_7} + j_7^{n_7})}$		k_7=2.1 j_7=0.16 n_7=4
	Autophosphorylation $v_{10} = k_8 * (1 - [pRIP3]) * \dfrac{[pRIP3]^{n_8}}{([pRIP3]^{n_8} + j_8^{n_8})}$		k_8=1.0 j_8=11.4 n_8=4
	Cleavage by *C8* in Complex-IIb $v_{11} = k_9 * [pRIP3] * \dfrac{[C8_{IIb}]^{n_9}}{([C8_{IIb}]^{n_9} + j_9^{n_9})}$		k_9=8.5 j_9=0.0015 n_9=4
	Degradation $v_{12} = d_3 * [pRIP3]$		d_3=0.14
$\dfrac{d[C8]}{dt} = F_{C8_{IIa}} + F_{C8_{IIb}}$ $F_{C8_{IIa}} = v_{13} - v_{16}$ $F_{C8_{IIb}} = v_{14} - v_{15} - v_{16}$	Activation by *acTRADD* in Complex-IIa $v_{13} = k_{10} * (1 - [C8]) * \dfrac{[acTRADD]^{n_{10}}}{([acTRADD]^{n_{10}} + j_{10}^{n_{10}})}$		k_{10}=3.6 j_{10}=1.25 n_{10}=4
	Activation by *pRIP1* in Complex-IIb $v_{14} = k_5 * (1 - [C8]) * \dfrac{[pRIP1]^{n_5}}{([pRIP1]^{n_5} + j_5^{n_5})}$		k_5=0.3 j_5=10.4 n_5=2
	Inhibition by *pRIP3* in Complex-IIb $v_{15} = k_6 * [C8_{IIb}] * \dfrac{[pRIP3]^{n_6}}{([pRIP3]^{n_6} + j_6^{n_6})}$		k_6=0.2 j_6=0.036 n_6=4
	Degradation $v_{16} = d_4 * [C8]$		d_4=0.35

930

931

932 **Kinetic parameters estimation**

933   Table of public experimental data sources for parameter estimation[12].

| This paper		Data Sources
Figure 1D	Figure 3F, 5F and S3B	
Figure 1F	Figure 5H	https://doi.org/10.1007/s13238-020-00810-x
Figure S1	Figure 5A, 5F and 5H	

934

935

936 **Supplemental Figures**

937
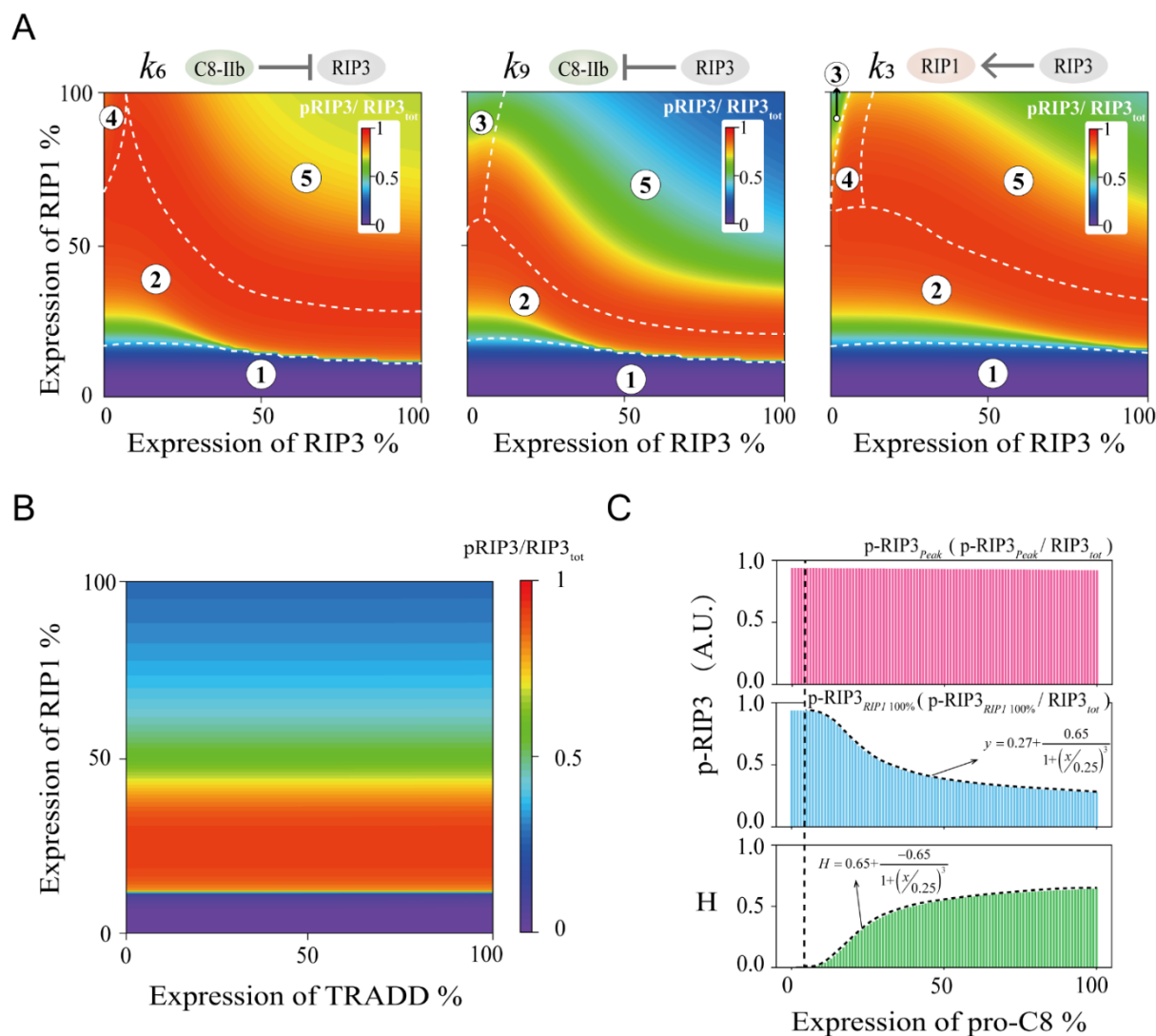
Figure S1. (A) The relative level of pRIP3 in the RIP3-RIP1 phase space when the terms of k6 (inhibition of C8 on pRIP3), k9 (the inhibition of pRIP3 on C8), and k3 (the positive feedback of pRIP3 on RIP1) are reduced 10-fold, respectively. (B) The relative level of pRIP3 in the TRADD-RIP1 phase space. (C) The variation of pRIP3Peak, pRIP3RIP1_100%, and H with pro-C8 expression level increases.

942

943
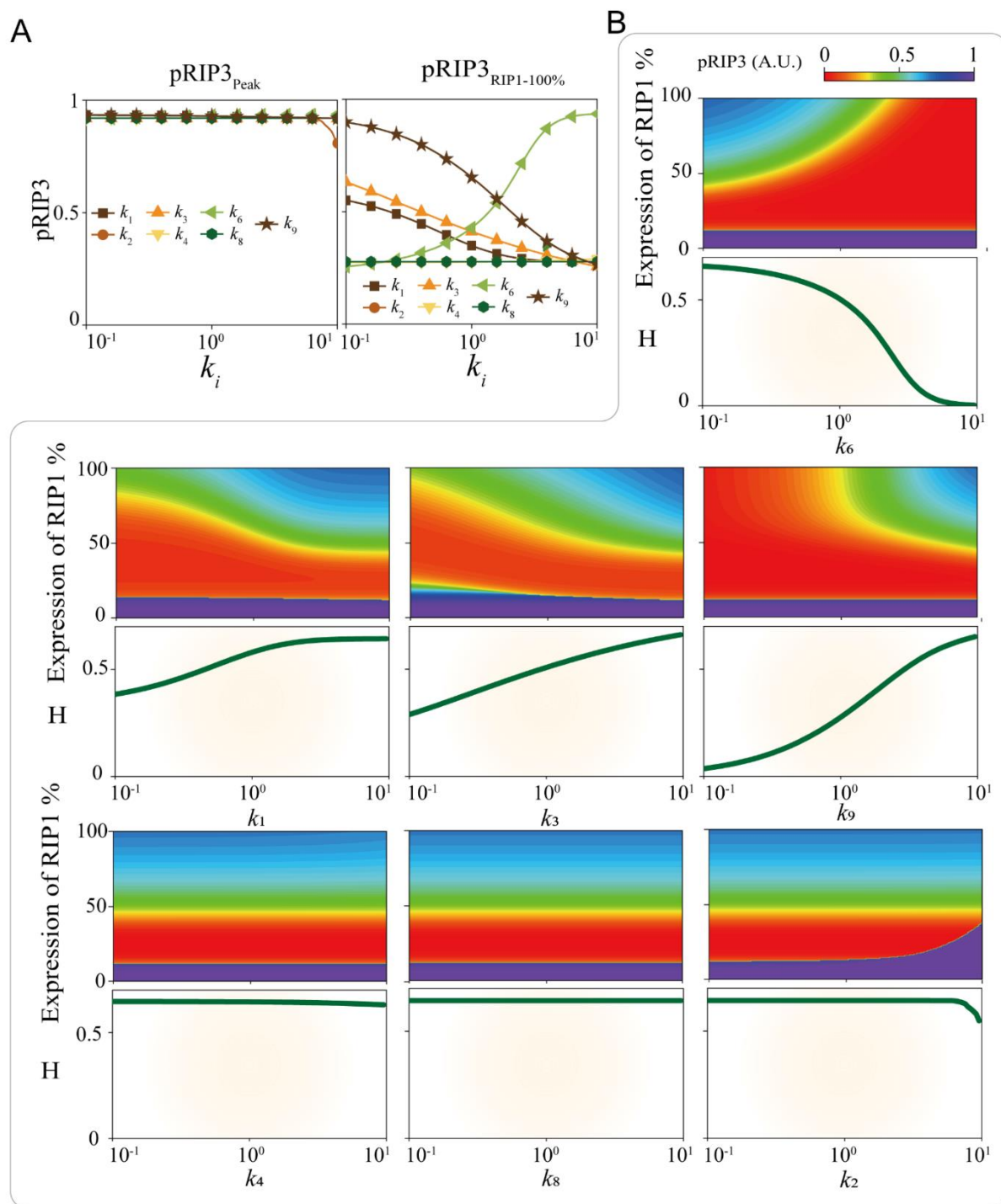
Figure S2. (A) Parameter sensitivity of other seven terms in modulating *pRIP3$_{peak}$* and *pRIP3$_{RIP1\_100\%}$*. (B) Analysis of

945 the seven terms regulations on pRIP3 and the scale of biphasic dynamics H.
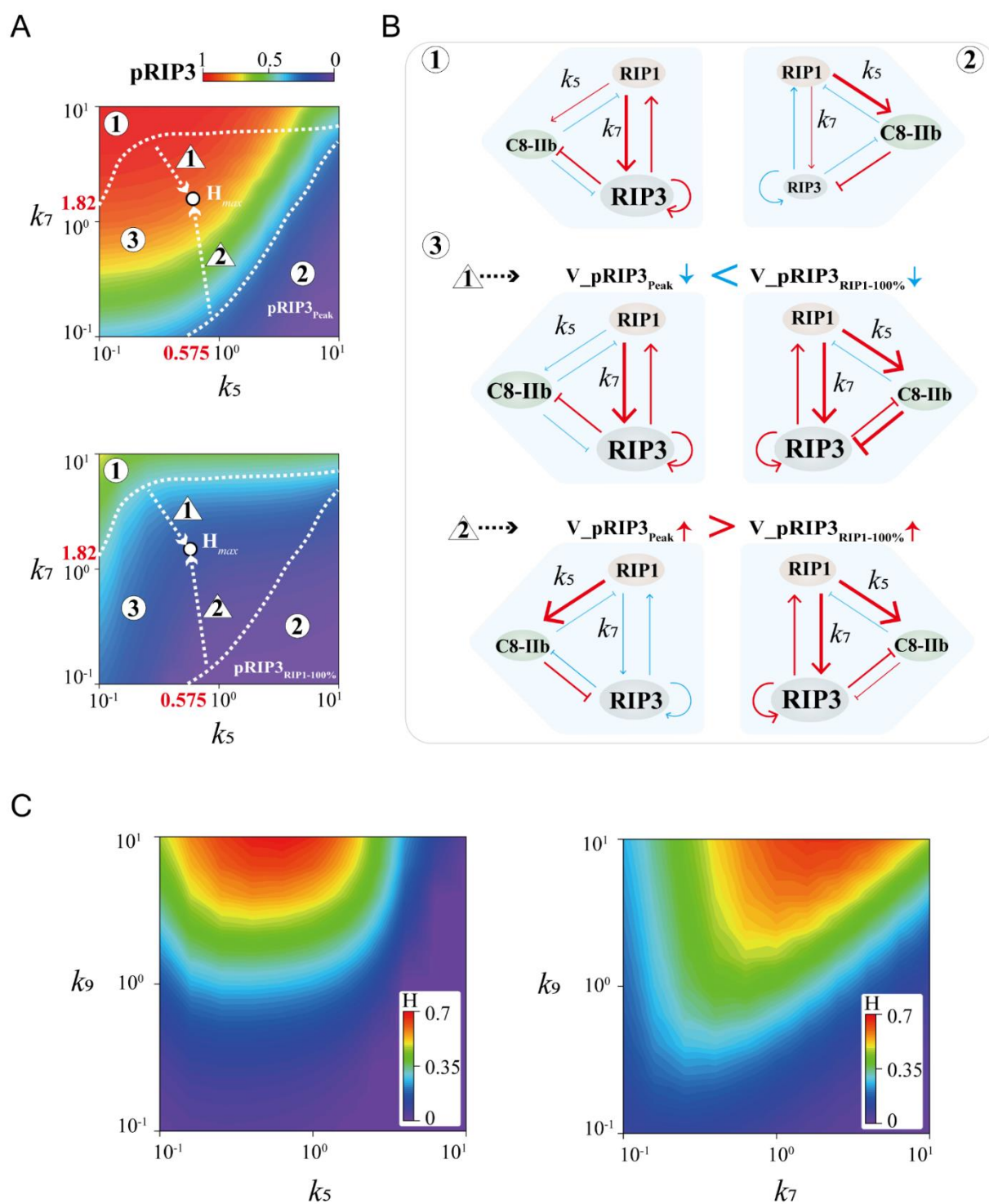
Figure S3. (A) Levels of $pRIP3_{peak}$ and $pRIP3_{RIP1\_100\%}$ in the k_5-k_7 parameter space, and the phase plane is decomposed into three regions and two processes. (B) Mechanistic analysis of k_5 and k_7 Bell-shaped regulation on pRIP3 biphasic dynamics. In regions 1 and 2, two terms, activation of RIP3 by RIP1 and activation of C8 by RIP1, play the dominant role, respectively. Their corresponding $pRIP3_{peak}$ and $pRIP3_{RIP1\_100\%}$ are both high or both low, resulting in small scales of biphasic dynamics. The decline rate of $pRIP3_{peak}$ in process 1 is lower than that of $pRIP3_{RIP1\_100\%}$, and the increase

952   rate of $pRIP3_{Peak}$ in process 2 is greater than that of $pRIP3_{RIP1\_100\%}$. (C) Phase diagram of H in k_5-k_7 and k_7-k_9 parameter

953   spaces.

954
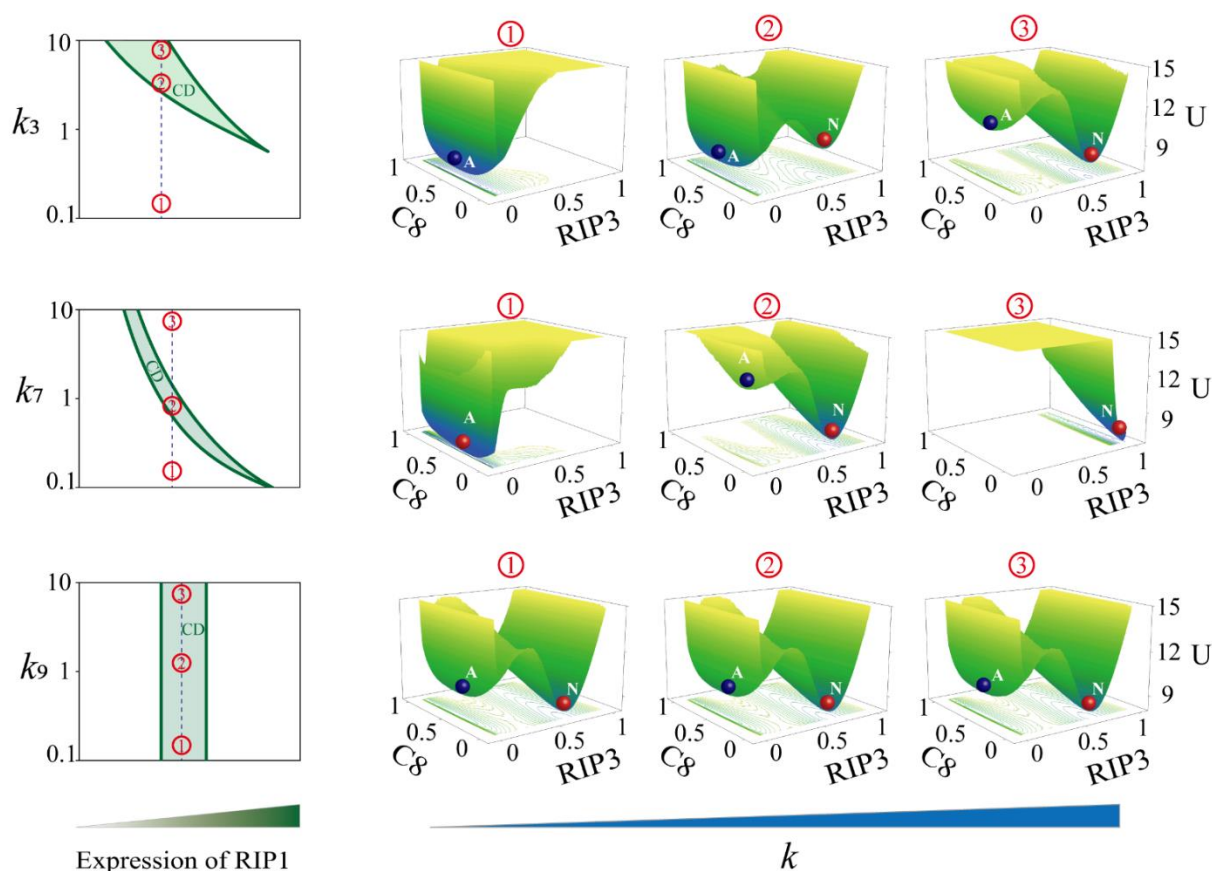
955

956   **Figure S4.** Phase diagram of the system stability on the co-variation of interaction term (k3, k7,

957   and k9) and the expression of RIP1. The green shaded region indicates the coexistence of apoptosis

958   and necroptosis. The potential energy landscape in C8-RIP3 phase space of the cell death system

959   at three typical values fixed for each parameter.

960
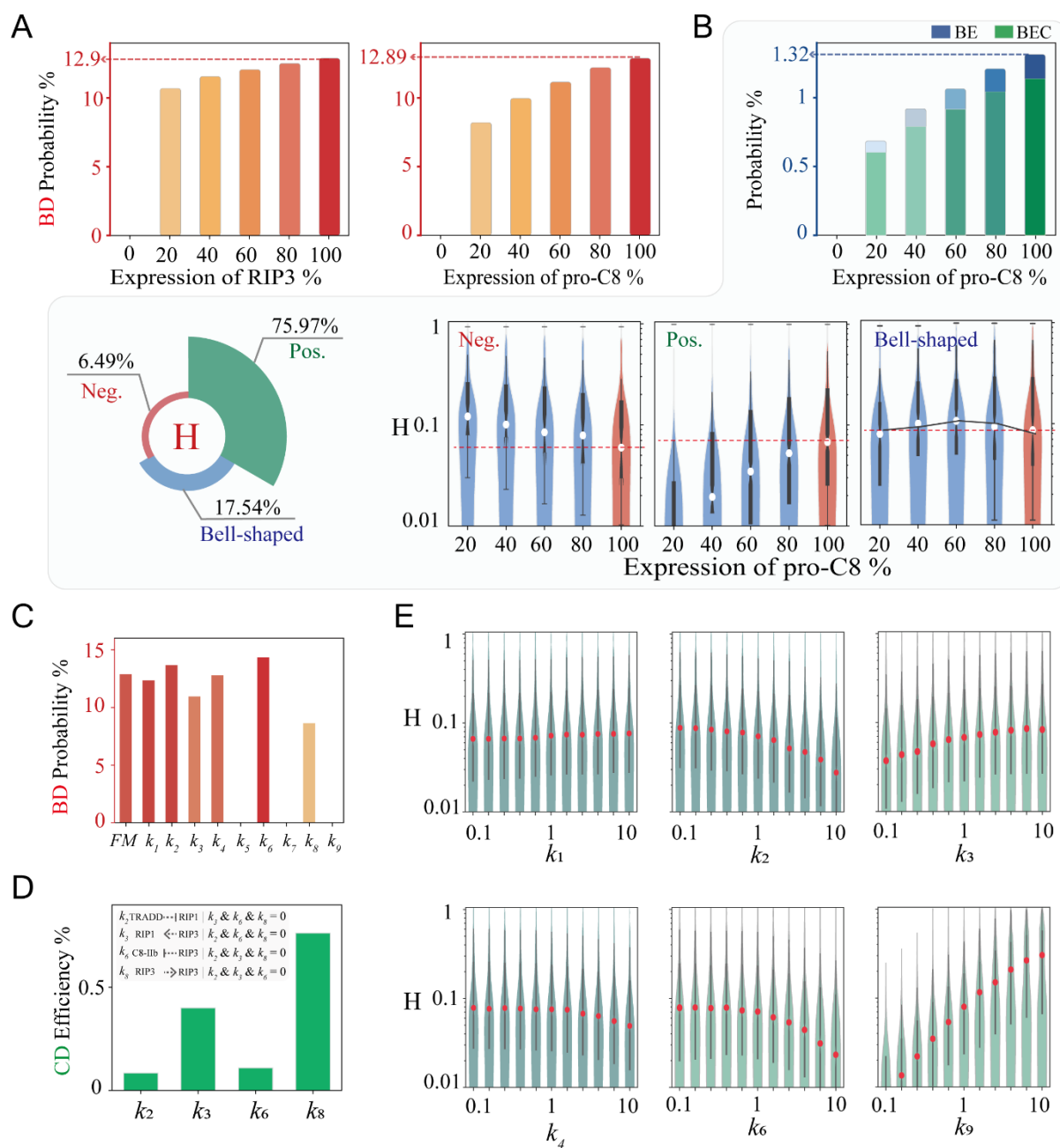
Figure S5. (A) Random circuit analysis with five representative RIP3 and pro-C8 expression levels to count the probabilities for achieving pRIP3 biphasic dynamics. (B) Random circuit analysis with five representative pro-C8 expression levels to count the probabilities for achieving pRIP3 BE and BEC dynamics, and the statistics of the regulatory behavior of RIP3 on the scale of biphasic dynamics H. (C) The probability of the system achieving biphasic dynamics when all interactions are blocked, respectively. (D) Contribution of all the positive feedback loops in circuit to achieve coexistence dynamics. (E) Statistics of the regulation of other six terms on H.
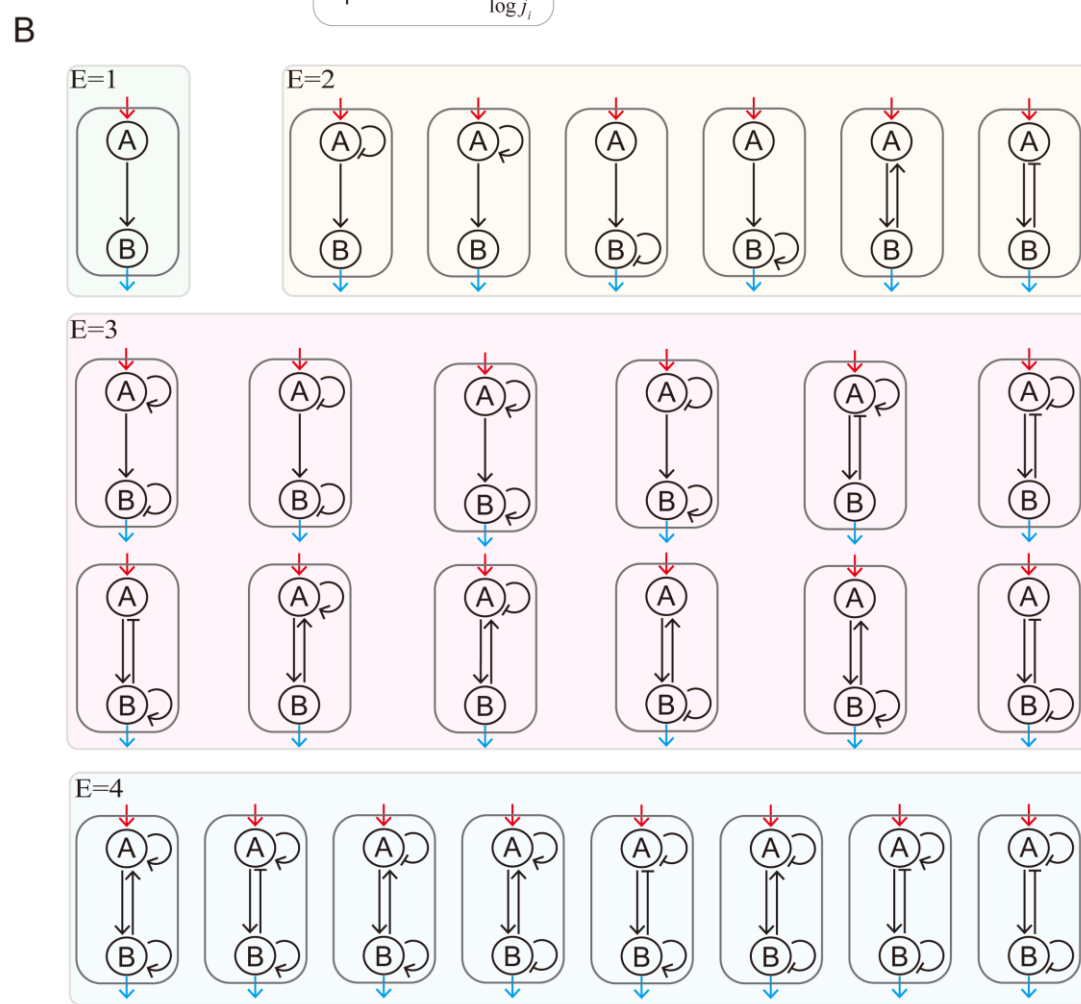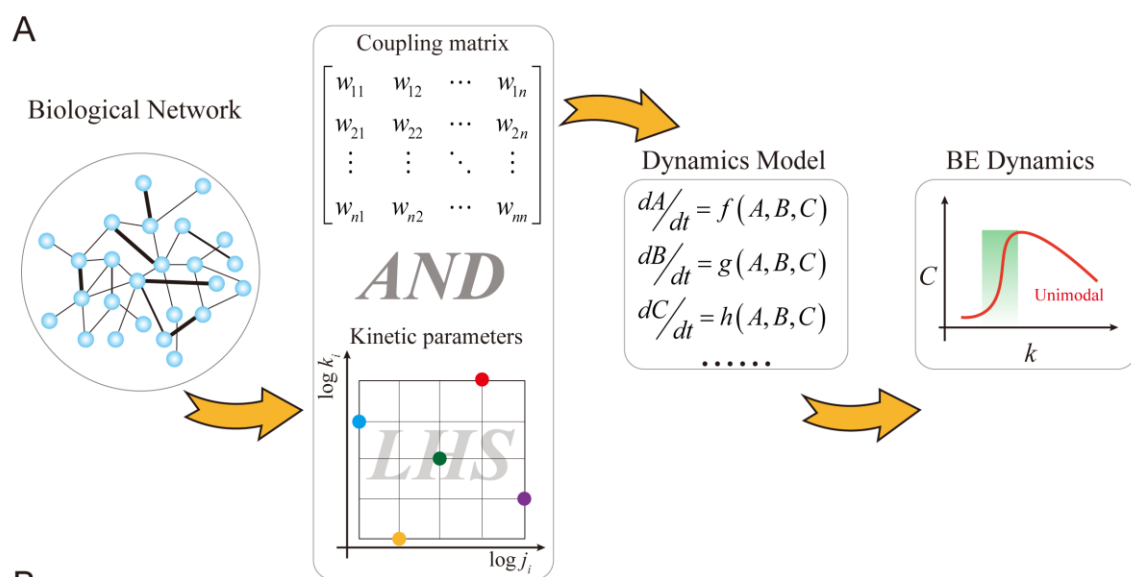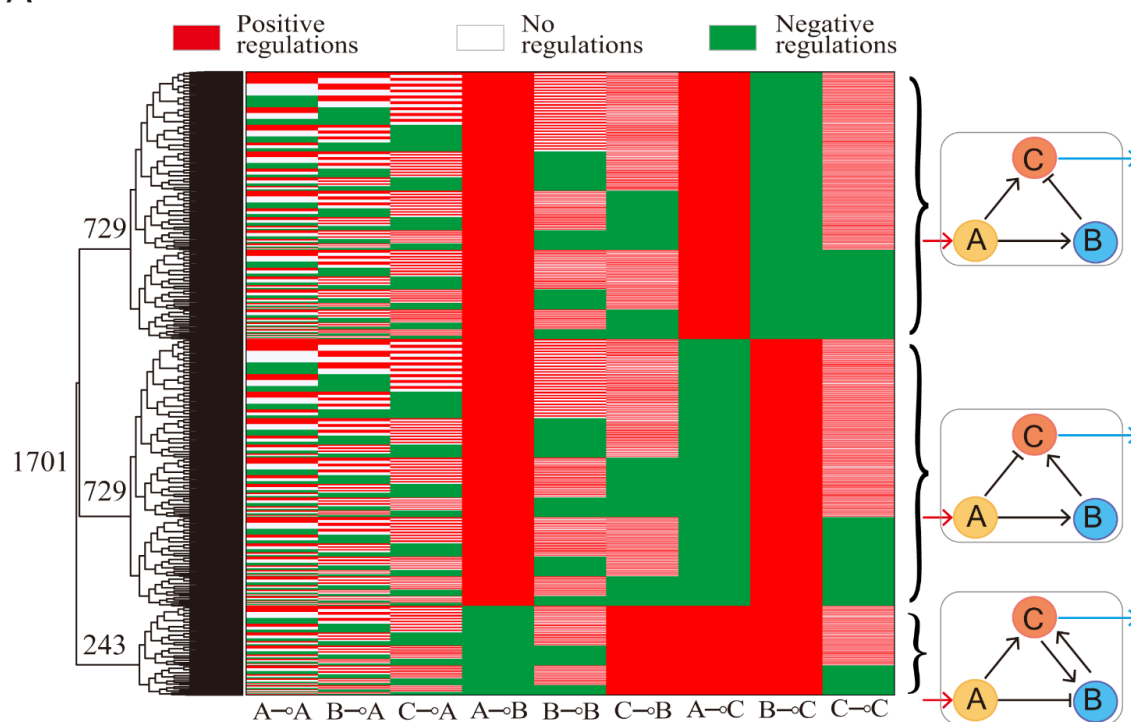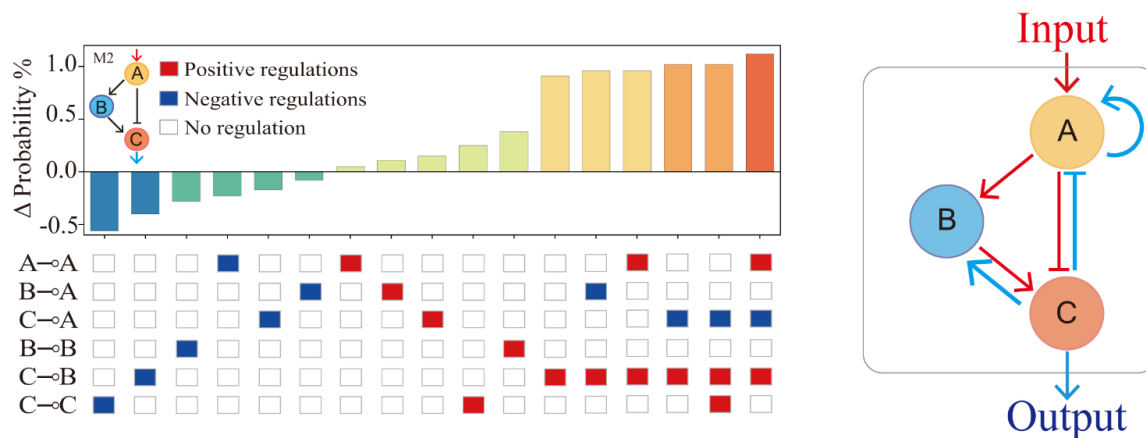
Figure S6. (A) Workflow for topology-to-function mapping of BE dynamics. (B) The 27 two-node motifs are classified according to the number of terms (connecting edges E).
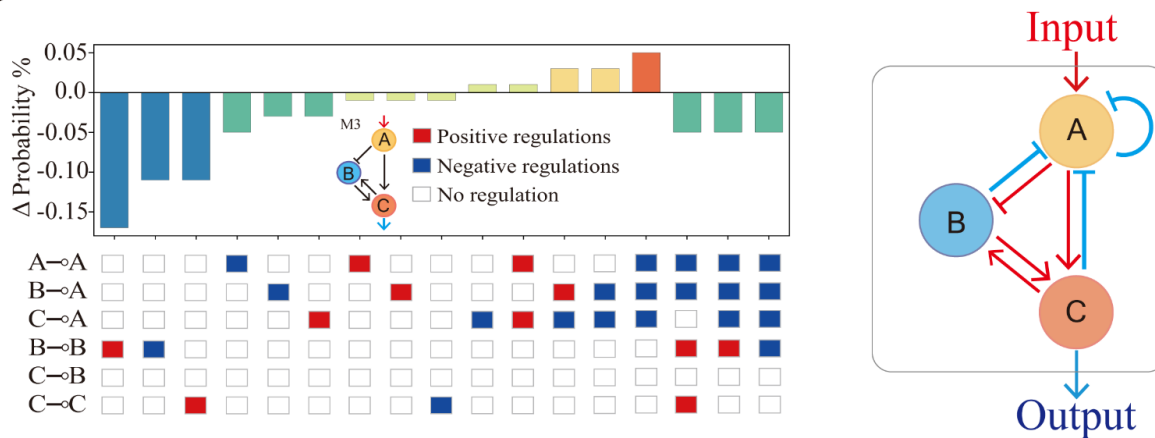
974

975 **Figure S7.** (A) Clustering of the 1,701 three-node circuits that can achieve BE dynamics. The core

976 circuits associated with each of the sub-cluster are shown on the right. (B) and (C) Probability

977 statistics of BE dynamics that can be achieved by randomly adding edges based on circuit M2 and

978 M3.

979

980